

# **Differentiation mechanism of the early Hadean mantle: insights from combined $^{176}\text{Hf}$ - $^{142,143}\text{Nd}$ signatures of Archean rocks from the Saglek Block.**

Précillia Morino<sup>1</sup>, Guillaume Caro<sup>1</sup>, Laurie Reisberg<sup>1</sup>

<sup>1</sup>Centre de Recherches Pétrographiques et Géochimiques (CRPG), UMR 7358, Université de Lorraine, CNRS, 54500 Vandœuvre-lès-Nancy, France.

\*Corresponding author: [pmorino@crpg.cnrs-nancy.fr](mailto:pmorino@crpg.cnrs-nancy.fr)

Abstract: 480 words

Main Text: 8046 words

13 items (9 Figures, 4 tables)

1 Appendix (online supplementary material)

## *Abstract*

*The presence of positive  $^{142}\text{Nd}$  anomalies in Eoarchean rocks provides evidence for early ( $4.40\pm0.03$  Ga; Morino et al., 2017) depletion of Earth's mantle. This model age lies within errors of the Pb-Pb "age of the Earth" (Connelly and Bizzarro, 2016), and is similar to model ages inferred for crystallization of the lunar mantle (McLeod et al., 2014), implying that this global event may reflect crystallization of a global magma ocean following the Moon-forming impact. However, the differentiation mechanism responsible for the formation of this early depleted reservoir and the depth at which it formed cannot be constrained from the Sm-Nd isotope system alone, because the magnitude of Sm/Nd fractionation during partial melting or fractional crystallization shows little dependence on pressure-controlled changes in mantle mineralogy. In contrast, the Lu-Hf isotope system is highly dependent on mineralogy, notably the presence or absence of garnet, an upper mantle phase, and thus*

may be used to constrain the pressure of fractionation. This study provides the first  $^{176}\text{Lu}$ - $^{176}\text{Hf}$  isotopic results on mafic and ultramafic rocks belonging to the Eoarchean (Nulliak) and Mesoarchean suites of the Saglek Block (northern Labrador, 3.2-3.9 Ga). The  $^{176}\text{Lu}$ - $^{176}\text{Hf}$  dating confirms the distinction between these two groups of rocks and provides ages consistent with those obtained from  $^{147}\text{Sm}$ - $^{143}\text{Nd}$  dating. The whole rock  $^{176}\text{Lu}$ - $^{176}\text{Hf}$  errorchrons yield ages and initial epsilon values of  $3766 \pm 140$  Ma,  $\epsilon^{176}\text{Hf}_i = 6.0 \pm 2.5$  and  $3023 \pm 390$  Ma,  $\epsilon^{176}\text{Hf}_i = -0.3 \pm 2.5$  for the Nulliak suite and the Mesoarchean suite respectively. The time-integrated  $^{176}\text{Lu}/^{177}\text{Hf}$  for the sources of the Nulliak and the Mesoarchean suites considering a time of differentiation at  $4.40 \pm 0.03$  Ga are estimated to be  $0.047 \pm 0.005$  and  $0.033 \pm 0.005$ , respectively. For the Mesoarchean samples, the combined  $^{146,147}\text{Sm}$ - $^{142,143}\text{Nd}$  and  $^{176}\text{Lu}$ - $^{176}\text{Hf}$  data are consistent with a near-chondritic mantle source. On the other hand, Nulliak ultramafic rocks were derived from a mantle reservoir with superchondritic Lu/Hf and Sm/Nd. The Nulliak parent reservoir, however, does not plot on the  $\epsilon^{176}\text{Hf}$ - $\epsilon^{143}\text{Nd}$  mantle array defined by modern oceanic basalts. Instead, the Nulliak source more likely belongs to a distinct array defined by Eo- and Meso-Archean komatiites. These results are interpreted in the framework of a simple model of crystallization of a primordial magma ocean. It appears that the fractionation observed in the mantle source of Nulliak was most likely generated by crystallization of a garnet-bearing assemblage in the shallow mantle, above the transition zone rather than by perovskite fractionation in the lower mantle. To preserve this depleted reservoir from the rest of the hot and vigorously convecting mantle, the Nulliak mantle source may have been isolated either at the top of the mantle in a buoyant lithosphere or near the core-mantle boundary, with the latter setting being more consistent with the komatiitic nature of the erupted rocks. Given that the garnet signature argues for differentiation of the Nulliak source at relatively shallow depth, its isolation in the deep mantle would require a cumulate overturn following crystallization of the magma ocean.

## 1. Introduction

Models of planet formation indicate that the final stage of Earth's accretion was punctuated by highly energetic collisions with planetary embryos (Chambers and Wetherill, 1998), following their rapid growth from a swarm of planetesimals (Chambers, 2004; Morbidelli et al., 2012). The last of these collisions (Canup and Asphaug, 2001), likely the Moon-forming impact, is believed to have induced large-scale melting of the proto-Earth's mantle, generating a global magma ocean that may have extended down to the core-mantle boundary (CMB) (Canup, 2004). Magma ocean crystallization could potentially have resulted in gross chemical stratification of Earth's mantle (Ohtani, 1985), sequestration of a basal molten layer near the CMB (Labrosse et al., 2007; Coltice et al., 2011) and the extraction of a primordial crust by upward migration of residual melts (Caro et al., 2005; Bourdon and Caro, 2007). Nevertheless, the long-term consequences of this event on the structure and composition of Earth's mantle, as well as the ultimate fate of primordial silicate reservoirs remain speculative, obscured by 4.5 Gyr of geodynamic activity and complete rejuvenation of Earth's surface. Our understanding of primary differentiation processes thus mainly relies on indirect observations based on short-lived radioactive decay systems (Caro et al., 2003; Touboul et al., 2012; Mukhopadhyay, 2012; Caracausi et al., 2016; Rizo et al., 2016; Mundl et al., 2017; Peters et al., 2018), which provide temporal and compositional information on primordial silicate reservoirs. One of these observations is that positive  $^{142}\text{Nd}$  anomalies (i.e. high  $^{142}\text{Nd}/^{144}\text{Nd}$  compared to the homogeneous value of the present-day mantle) are present in Archean terranes of West Greenland and Northern Canada (Caro et al., 2006; Bennett et al., 2007; Rizo et al., 2012; Debaille et al., 2013; Morino et al., 2017). Such anomalies were produced by decay of now extinct  $^{146}\text{Sm}$  ( $T_{1/2}=103$  Myr) in a mantle reservoir that was depleted in incompatible elements near the end of terrestrial accretion, at  $4.40\pm0.03$  Ga (Morino et al., 2017). This reservoir (hereafter referred to as Early Depleted Mantle or EDM) was episodically sampled by Archean magmatism at least until 2.7 Gyr ago (Debaille et al., 2013). Model age calculations using coupled  $^{146,147}\text{Sm}$ - $^{142,143}\text{Nd}$  chronometry indicate that the differentiation event responsible for the formation of the EDM predated late-stage crystallization of the lunar magma ocean by  $<50$  Ma (Solomon and Longhi, 1977; Boyet and Carlson, 2007; Borg et al., 2011; Elkins-Tanton et al., 2011; McLeod et al., 2014). This time interval is consistent with slower cooling of the residual

lunar magma ocean under the blanketing effect of a thick anorthositic crust (Elkins-Tanton et al., 2011). The  $^{146,147}\text{Sm}$ - $^{142,143}\text{Nd}$  age of the EDM also lies within error of the Pb-Pb age of the Earth, at ca.  $4.42 \pm 0.01$  Ga (Connelly and Bizzarro, 2016), which was suggested to record Pb loss by devolatilization or by sequestration in the core during the giant impact phase of accretion (Oversby and Ringwood, 1971; Wood et al., 2006; Lagos et al., 2008; Wood et al., 2010; Connelly and Bizzarro, 2016). Collectively, these chronological constraints point towards a major differentiation event at ca. 4.40 Ga, possibly triggered by the Moon-forming impact, and ultimately resulting in global chemical differentiation of the mantle-crust system.

While the chronological aspects of early mantle differentiation are well established from coupled  $^{146,147}\text{Sm}$ - $^{142,143}\text{Nd}$  systematics, fundamental uncertainties still remain as to the physical process that produced the depleted reservoir carrying positive  $^{142}\text{Nd}$  anomalies. Preservation of primordial mantle domains on a billion year timescale requires long-term isolation from the convective system (Morino et al., 2017). This observation is consistent with creation of positive  $^{142}\text{Nd}$  anomalies in a chemically buoyant lithospheric mantle, which may have been preserved from rehomogenization as part of a long-lived Hadean stagnant lid (Debaille et al., 2013; Caro et al., 2017). Alternatively, the presence of positive  $^{142}\text{Nd}$  anomalies in Eoarchean rocks may reflect entrainment within hot plumes of perovskitic cumulates formed by fractional crystallization of a basal magma ocean (Labrosse et al., 2007). The  $^{146,147}\text{Sm}$ - $^{142,143}\text{Nd}$  systems alone cannot provide definitive constraints on this issue because the magnitude of Sm/Nd fractionation during partial melting or fractional crystallization shows little dependence on pressure-controlled changes in mantle mineralogy, i.e., Sm is less incompatible than Nd throughout the mantle, so cumulates with moderately elevated Sm/Nd would be produced at all mantle depths. To circumvent this limitation, Caro et al. (2005) proposed an approach based on coupled  $^{146,147}\text{Sm}$ - $^{142,143}\text{Nd}$  and  $^{176}\text{Lu}$ - $^{176}\text{Hf}$  systematics, with the aim of fingerprinting the crystallization of Mg-perovskite (bridgmanite) at lower mantle pressures. Unlike Sm/Nd, Lu/Hf partitioning is strongly dependent on mantle mineralogy (e.g. Salters and White, 1998; Corgne and Wood, 2004). At upper mantle pressures pertaining to partial melting and/or fractional crystallization in the presence of garnet, Lu is less incompatible than Hf.

Crystallization of a shallow (<660 km) magma ocean is thus expected to generate positively correlated Lu/Hf and Sm/Nd fractionations, provided that melt segregation proceeded faster than upward migration of the solidification front (Solomatov and Moresi, 1996; Solomatov and Louis, 2007). In contrast, at lower mantle pressures in the presence of bridgmanite, Hf becomes more compatible than Lu (Corgne et al., 2004), so that crystallization of a deep magma ocean is expected to produce negatively correlated Lu/Hf and Sm/Nd fractionations (Caro et al., 2005). The  $^{176}\text{Hf}$ - $^{143}\text{Nd}$  signatures of Eoarchean rocks carrying  $^{142}\text{Nd}$  anomalies, which ultimately reflect the time-integrated Lu/Hf and Sm/Nd of their sources, thus have the potential to provide important constraints on the depth and processes pertaining to differentiation of the EDM.

The approach outlined above requires determination of both the Sm/Nd and Lu/Hf of the mantle reservoir hosting the positive  $^{142}\text{Nd}$  anomaly. While the former can be precisely determined from coupled  $^{146,147}\text{Sm}$ - $^{142,143}\text{Nd}$  systematics (Caro et al., 2003; Caro et al., 2006; Bennett et al., 2007; Rizo et al., 2011; Rizo et al., 2012; O'Neil et al., 2016), previous attempts to estimate  $(\text{Lu}/\text{Hf})_{\text{EDM}}$  from Eoarchean mafic rocks of the Isua Supracrustal Belt (ISB, West Greenland; 3.7-3.8 Ga) yielded conflicting results. Rizo et al. (2011) and Hoffmann et al. (2011) reported unradiogenic initial  $^{176}\text{Hf}/^{177}\text{Hf}$  signatures in amphibolites of tholeiitic affinity sampled in the northwestern section of the ISB. This result, indicative of a subchondritic  $(\text{Lu}/\text{Hf})_{\text{EDM}}$ , is consistent with melting of cumulates mainly composed of bridgmanite, suggesting derivation of ISB metabasalts from a deep mantle source (Rizo et al., 2011). At odds with this interpretation, Hoffmann et al. (2010) reported highly radiogenic initial  $^{176}\text{Hf}/^{177}\text{Hf}$  in boninite-like metabasalts situated in the Eastern section of the ISB. This radiogenic signature requires a mantle source with superchondritic Lu/Hf, seemingly more consistent with its prior depletion in the garnet stability field. Remarkably, both magmatic series are characterized by a positive  $^{142}\text{Nd}$  anomaly averaging +10 ppm (Caro et al., 2006; Hoffmann et al., 2010; Rizo et al., 2011; O'Neil et al., 2016), and yielded similar time-integrated  $^{147}\text{Sm}/^{144}\text{Nd}$  source ratios (ca. 0.210-0.215). Hoffmann et al. (2011) suggested that decoupling of  $^{176}\text{Lu}$ - $^{176}\text{Hf}$  and  $^{147}\text{Sm}$ - $^{143}\text{Nd}$  systems in Isua meta-tholeiites may reflect contamination of their source by detrital metasediments with low Lu/Hf recycled in a proto-subduction zone, rather than a pristine signature

from a deep perovskitic reservoir. Conversely, the highly radiogenic  $^{176}\text{Hf}/^{177}\text{Hf}$  measured in boninite-like amphibolites may indicate contamination of their source by LREE-poor chemical sediments characterized by high Lu/Hf (e.g. cherts), as suggested by Blichert-Toft et al. (2015) to explain the apparent decoupling of  $^{176}\text{Hf}$ - $^{143}\text{Nd}$  signatures in South African komatiites.

The Eoarchean Nulliak suite of the Saglek Block (Labrador, Canada), constituted of mafic and ultramafic rocks, provides an opportunity to test these scenarios and better constrain the geodynamic evolution of the EDM following solidification of the magma ocean. Unlike many occurrences of ultramafic rocks in Eoarchean terranes, the Nulliak suite underwent only partial serpentinization, and yielded a precise  $^{147}\text{Sm}$ - $^{143}\text{Nd}$  isochron age and initial  $^{143}\text{Nd}/^{144}\text{Nd}$  (Morino et al., 2017). All mafic and ultramafic rocks of the Nulliak assemblage exhibit a homogeneous  $^{142}\text{Nd}$  anomaly of  $8\pm 3$  ppm, allowing calculation of a model age of differentiation for their mantle source at  $4.40\pm 0.03$  Ga with a time-integrated  $^{147}\text{Sm}/^{144}\text{Nd}$  of 0.211. In this study, we present the first  $^{176}\text{Lu}$ - $^{176}\text{Hf}$  isotopic data for mafic and ultramafic rocks of the Saglek block, using the two sample suites previously analyzed for  $^{146,147}\text{Sm}$ - $^{142,143}\text{Nd}$  by Morino et al. (2017). We show that the Nulliak source composition inferred from  $^{176}\text{Lu}$ - $^{176}\text{Hf}$  and  $^{146,147}\text{Sm}$ - $^{142,143}\text{Nd}$  systematics can be reproduced by crystallization of a shallow magma ocean in the garnet stability field.

## 2. Samples and Geologic Setting

The samples analyzed in this study were collected during fieldwork in the Hebron-Saglek fjord region of the Saglek block (3.2-3.9 Ga, northern Labrador, Canada). Regional geology and prior geochronological work were summarized in several previous studies (e.g. Schiøtte et al., 1989, Bridgwater and Schiøtte, 1991; Schiøtte et al., 1992; Komiya et al., 2015; Morino et al., 2017). Geographic locations, as well as major and trace element compositions of our samples, are provided in Morino et al. (2017). The Saglek block (Fig 1) is located near the northern extremity of the Labrador Peninsula, across from the Akuleq terrane of Southwest Greenland, and represents the westernmost part of the North Atlantic craton. The Saglek block is divided into two tectonic domains separated by

the NS-trending, subvertical Handy Fault (Ryan and Martineau, 2012). The western domain underwent high grade metamorphism in the granulite facies at ca. 2.7-2.8 Ga, while the eastern domain is primarily characterized by amphibolite facies metamorphism (Ryan and Martineau, 2012). Both domains are dominated by Eoarchean quartzofeldspathic gneisses of the Uivak suite (3.6-3.9 Ga) with a subordinate Mesoarchean component (the Lister gneisses, 3.2 Ga) and late (ca. 2.4 Ga) intrusions of post-tectonic granitoids (Komiya et al., 2015; Shimojo et al., 2016). Numerous volcano-sedimentary enclaves are present in the area, embedded in Eoarchean gneisses of the Uivak suite (Ryan and Martineau, 2012). On the basis of field relationships of supracrustal rocks with the Mesoarchean Saglek dyke swarm, Bridgwater and Schiøtte (1991) and Ryan and Martineau (2012) proposed a subdivision of these units into an Eoarchean group called the Nulliak assemblage, and a Mesoarchean group called the Upernavik formation. On the basis of whole-rock  $^{147}\text{Sm}$ - $^{143}\text{Nd}$ ,  $^{187}\text{Re}$ - $^{187}\text{Os}$  and U-Pb zircon dating, the emplacement age of the Nulliak assemblage was estimated to be 3.6-4.0 Ga (Collerson et al., 1991, Schiøtte et al., 1992, Ishikawa et al., 2017, Morino et al., 2017). The emplacement age of Upernavik supracrustal rocks remains poorly constrained but is likely between 3.1 and 3.4 Ga (Schiøtte et al., 1992, Morino et al., 2017, Ishikawa et al., 2017).

Our sample set includes 15 ultramafic rocks (4 metadunites, 11 metapyroxenites) and 5 amphibolites collected east of the Handy fault, in the vicinity of Jerusalem Harbour and along the coast north of Iterugnek fjord. In the field, mafic/ultramafic rocks occur either as monolithological meter-sized enclaves (LA9 series) or as larger (50-500 m) mafic/ultramafic units (LA11 and LA8 series) enclosed in granitoid gneisses of the Uivak suite. The samples were further divided into two groups on the basis of their  $^{146}\text{Sm}$ - $^{142}\text{Nd}$  and  $^{147}\text{Sm}$ - $^{143}\text{Nd}$  systematics (Morino et al 2017). A first group, which displays a positive  $^{142}\text{Nd}$  anomaly of  $+8\pm 3$  ppm, yielded a  $^{147}\text{Sm}$ - $^{143}\text{Nd}$  whole-rock isochron age of  $3.78\pm 0.09$  Ga and was thus assigned to the Eoarchean Nulliak assemblage. The second group, without  $^{142}\text{Nd}$  anomaly, yielded a  $^{147}\text{Sm}$ - $^{143}\text{Nd}$  isochron age of  $3.36\pm 0.10$  Ga and was tentatively assigned to the Mesoarchean Upernavik formation.

Although primary textures indicative of a volcanic origin were not preserved, ultramafic rocks from both the Meso- and Eoarchean suites exhibit geochemical characteristics consistent with

differentiation of komatiitic lavas (Morino et al 2017). Using a previously established komatiite classification scheme (Nesbitt and Su, 1979), ultramafic rocks were therefore divided into Al-depleted, Al-undepleted and Al-enriched subgroups according to their major and trace element compositions (Morino et al 2017).

### 3. Metasomatic alteration and crustal contamination

Supracrustal rocks of the Saglek block have undergone poly-phase metamorphism in the amphibolite to granulite facies, as well as metasomatic alteration. These events resulted in extensive recrystallization, serpentinization and redistribution of fluid mobile elements (e.g. U, Ba, Rb, K) from the surrounding granitoid gneisses to the ultramafic protoliths (Liu et al., 2016, Morino et al, 2017). The geochemical effects of post-emplacement alteration are broadly similar to those reported in mafic rocks (amphibolites) of the Isua Supracrustal Belt (Polat and Hofmann, 2003). In plots of selected REE (Rare Earth Elements) and HFSE (High Field Strength Elements) versus immobile trace elements such as Zr, samples of the Meso- and Eoarchean suites display systematic variations (Fig 2 A-D) reflecting preserved magmatic differentiation trends. This observation is consistent with the limited mobility of HFSE and REE during metamorphism. For the Eoarchean suite, excluding possibly contaminated samples (see below), correlation coefficients (R) in binary plots versus Zr tend to decrease from the heavy and intermediate REE (Lu: R=0.87, Sm: R=0.97) to the light REE (Nd: R=0.73, La: R=0.22) reflecting the higher mobility of LREE during metamorphism. This effect is however less pronounced for the Mesoarchean suite (R>0.95 for Sm, Lu, Nd; R=0.83 for La). All HFSE are tightly correlated with Zr (Hf: R>0.99 for both the Meso- and Eoarchean suites) indicating little post-magmatic mobility. In contrast, secondary enrichments in Th and U are evident in both Meso- and Eoarchean samples (Fig. 2 E-F), consistent with the previously reported mobility of these elements in high grade metamorphic terranes (Polat and Hofmann, 2003).

The effects of crustal contamination on the trace element composition of Saglek ultramafic rocks are illustrated in Figure 3, using  $(Ce/Yb)_N$  as a measure of LREE enrichment (the subscript N indicates normalization to primitive mantle values of McDonough and Sun (1995)). The extent of crustal assimilation is difficult to assess with confidence due to superimposed chemical variability



induced by metasomatism, fractionation during melt extraction and intrinsic source heterogeneities. Based on literature data, uncontaminated komatiites, nevertheless, define compositional domains in plots of selected trace element ratios versus  $(\text{Ce/Yb})_N$ , which can be used to screen for anomalous LREE enrichment (Fig 3). These komatiites exhibit flat to depleted trace element patterns, with  $(\text{Ce/Yb})_N < 2$ ,  $(\text{Sm/Nd})_N = 0.8-2$ ,  $(\text{Th/La})_N = 0.5-1$  and  $(\text{Nb/La})_N \approx 1$ . Crustal contamination is expected to translate into LREE enrichment, pronounced negative Nb anomalies and variable enrichment in highly incompatible elements such as Th and U (e.g. Puchtel et al., 2016). On the basis of their Ce/Yb ratio, and the binary plots of Figure 2, it appears that two samples of the Eoarchean suite (LA9-18 and LA9-19) and one sample of the Mesoarchean suite (LA11-14) may have been affected by crustal contamination. Both Eoarchean samples display a marked enrichment in LREE with  $(\text{Ce/Yb})_N = 3-4$  and  $(\text{Sm/Nd})_N \approx 0.7$  (Fig. 3) as well as anomalously high Zr (and other incompatible elements) contents, consistent with assimilation of felsic material. Both samples also plot above magmatic differentiation trends in diagrams of Hf, Sm and Nd versus MgO. Aside from these two samples, however, ultramafic rocks from the Nulliak group display highly depleted LREE signatures (Fig 3A) and therefore show no compelling evidence of crustal assimilation. Mesoarchean samples exhibit slightly higher  $(\text{Ce/Yb})_N$ , typically between 1.5 and 2, but, with the exception of LA11-14, all samples remain within the compositional range defined by Barberton and Abitibi komatiites. Both the Meso- and Eoarchean suites also exhibit variable but generally high  $(\text{Th/La})_N$  and low  $(\text{Nb/La})_N$  compared to typical komatiite values (Fig 3). However, neither ratio correlate with  $(\text{Ce/Yb})_N$ . Given the poor correlations between Zr and La and Th (Fig. 2E), we interpret these anomalous signatures to reflect Th and La redistribution during metasomatism associated with Neoproterozoic metamorphism rather than pervasive crustal contamination.

The variability of Lu/Hf values in Saglek ultramafic rocks is similar to that observed in Archean komatiites (Fig 4) and can thus be interpreted in terms of trace element fractionation during melt extraction. As shown in Figure 4, Lu/Hf in the Meso- and Eoarchean suites displays a positive correlation with  $\text{Al}_2\text{O}_3/\text{TiO}_2$  (and a negative correlation with Gd/Yb), consistent with a primary control by the garnet component of their mantle source. The Al-depleted samples ( $\text{Al}_2\text{O}_3/\text{TiO}_2 \approx 5-11$ ) have the

lowest (Lu/Hf)<sub>N</sub> values (0.2-0.7) because garnet is not exhausted from the mantle source during partial melting, and strongly retains Lu relative to Hf (e.g. Robin-Popieul et al., 2012). For Eoarchean Al-depleted samples, this primary fractionation may have been accentuated by assimilation of crustal material with low Lu/Hf. In contrast, Al-enriched samples (Al<sub>2</sub>O<sub>3</sub>/TiO<sub>2</sub>≈30-50), derived from garnet-rich residues produced by prior extraction of low Al<sub>2</sub>O<sub>3</sub>/TiO<sub>2</sub> melts, have the highest (Lu/Hf)<sub>N</sub> values (1.5-3). The Al-undepleted type (Al<sub>2</sub>O<sub>3</sub>/TiO<sub>2</sub>≈15-25) is characterized by near-primitive (Lu/Hf)<sub>N</sub>, reflecting first-stage melting above the garnet solidus.

#### 4. Analytical procedure

Lutetium and Hafnium isotopic analyses were performed on 15 ultramafic and 5 mafic rocks previously analyzed for <sup>146,147</sup>Sm-<sup>142,143</sup>Nd by Morino et al (2017). Different digestion aliquots from the same bulk powder were used for <sup>176</sup>Lu-<sup>176</sup>Hf and <sup>147</sup>Sm-<sup>143</sup>Nd analyses. Chemical separation of these elements was done in a controlled-air clean lab under a HEPA filtered laminar flow hood using equipment previously cleaned in HF. A mixed <sup>176</sup>Lu-<sup>180</sup>Hf spike was added to 100-300 mg whole rock powder and dissolved in a HNO<sub>3</sub>-HF mixture (1:1). The digestion was carried out in high-pressure PTFE/TFM BOLA bombs heated in an oven during 3 days at 150°C (Luais et al., 2009). The solutions were then slowly evaporated on a hot plate and the residues dissolved in 5 ml of 6 N HCl, after which the bombs were replaced in the oven for 3 days at 150°C. Lastly, the dissolved samples were transferred into Savillex vials and dried down then redissolved in 4 N HCl to break down residual fluorides. This final step was repeated several times until a perfectly clear solution was obtained.

Hafnium and Lutetium were separated from the rock matrix using a single-column procedure (Table 1) adapted from Munker et al. (2001), Wimpenny et al. (2013) and Yang et al. (2010). Upon complete dissolution of fluoride precipitates, samples were dried, dissolved in 5 mL of 3 N HCl + 0.1 N ascorbic acid and introduced onto 1.8 mL Bio-Rad Poly-Prep columns filled with LN resin (50-100 mesh, Eichrom technologies). The matrix and most of the REE were first eluted in 3 N HCl, after which Yb and Lu were eluted in 10 mL of 3.4 N HCl and 10 mL of 6 N HCl, respectively. Titanium was then rinsed off as a peroxide complex with up to 50 mL of a 3 N HNO<sub>3</sub> + 0.5% H<sub>2</sub>O<sub>2</sub> mixture, after which Hf and Zr were collected in 2 mL of 2 N HF. This protocol allows separation of the bulk

of Yb from the Lu fraction, thereby reducing uncertainties related to isobaric interference correction on  $^{176}\text{Lu}$ . The Ti/Hf in the final Hf cut was typically between 0.3 and 1, down from 300-600 in ultramafic rocks and 270-400 in mafic rocks. Tests performed using synthetic solutions with variable Ti/Hf ( $\approx 0.5$  to 200) confirmed that at such low levels, the presence of Ti has no significant effect on the accuracy and reproducibility of  $^{176}\text{Hf}/^{177}\text{Hf}$  measurements. The analysis of mixed standard solutions with Zr/Hf=35 also showed that the presence of Zr has no effect on measured  $^{176}\text{Hf}/^{177}\text{Hf}$  values. Total procedural blanks measured for each purification were <50 pg for both Lu and Hf and chemistry yields were 80-90% for Lu and >90% for Hf.

Hafnium isotopes were analyzed on a Thermo Scientific *Neptune Plus* MC-ICPMS equipped with an Apex-HF inlet system (Elemental Scientific) and standard skimmer and sampler cones. Prior to analysis, the Hf separate was dissolved in 1 mL of 0.5 N  $\text{HNO}_3$  - 0.3 N HF. An aliquot of this solution was used to estimate the approximate Hf concentration of the sample, after which the solution was diluted to a concentration of 100 ppb, typically yielding a  $^{177}\text{Hf}$  signal of 4 V on  $10^{11} \Omega$  amplifiers. Hafnium isotopes were measured in static multicollection in low resolution mode (Table 2), collecting 50 cycles with an integration time of 4.194 s. per cycle. Baselines were measured prior to each analysis with an integration time of 30 s. Potential isobaric interferences at mass 176 were monitored by collecting  $^{172}\text{Yb}$  and  $^{175}\text{Lu}$  in cups L4 and L2, respectively, and corrected offline using  $^{172}\text{Yb}/^{176}\text{Yb}=1.711$  and  $^{175}\text{Lu}/^{176}\text{Lu}=37.666$  (Vervoort, 2013; Vervoort et al., 2004). However, neither Lu nor Yb were found in significant amounts ( $^{172}\text{Yb}/^{176}\text{Hf} < 2.5 \times 10^{-4}$  and  $^{175}\text{Lu}/^{176}\text{Hf} < 5 \times 10^{-4}$  in all cases) in the Hf separates following the chemical procedure and these corrections were always negligible. Likewise, neither W nor Ta were detected in Hf separates after chemical purification and thus no correction was applied for potential interferences at mass 180. The instrumental blank was measured for 40 s. prior to each sample or standard analysis, following a 6 minute wash period in 0.6 N HF-1 N  $\text{HNO}_3$  (3 min.) and in 0.3 N HF-0.5 N  $\text{HNO}_3$  (3 min.), and was subtracted offline from the following sample/standard analysis. Instrumental mass discrimination was corrected by bracketing using the Nancy Ames standard, whose isotopic composition ( $^{176}\text{Hf}/^{177}\text{Hf}_{\text{Ames}}=0.282243 \pm 0.0000013$  2S.D., n=30) was anchored to a  $^{176}\text{Hf}/^{177}\text{Hf}$  value of  $0.282156 \pm 0.000008$  (2S.D., n=21) for the inter-

laboratory JMC-475 standard. The  $^{176}\text{Hf}/^{177}\text{Hf}$  value for the JMC-475 standard is consistent with the accepted value of 0.282160 determined by Blichert-toft (2001).

The analytical protocol for Lu isotope measurements is similar to that used for Hafnium (Table 2). The Lu separate was dissolved in 2%  $\text{HNO}_3$  and diluted to a concentration of 20 ppb, equivalent to a 3.5 V signal on  $^{175}\text{Lu}$ . Instrumental mass fractionation was corrected by bracketing using the NIST standard reference material 3132a, which yielded an average  $^{175}\text{Lu}/^{176}\text{Lu}$  value of  $0.0265732 \pm 0.0000055$  (2SD,  $n=15$ ) similar within errors to the natural value obtained by Blichert-Toft et al. (1997). The Yb-Lu interference at mass 176 was monitored by collecting  $^{173}\text{Yb}$  and corrected offline using  $^{176}\text{Yb}/^{173}\text{Yb}=0.79639$ . The potential isobaric interference from  $^{176}\text{Hf}$  was monitored using  $^{177}\text{Hf}$  and corrected using  $^{176}\text{Hf}/^{177}\text{Hf}=0.282160$  (Vervoort, 2015). However, no detectable amount of Hf was found in the Lu separates following chemistry. Instrumental blanks were measured for 40 seconds prior to sample analysis following a 6 minute wash in 2%  $\text{HNO}_3$ .

The precision and accuracy of  $^{176}\text{Hf}/^{177}\text{Hf}$  and  $^{176}\text{Lu}/^{177}\text{Hf}$  determination was monitored by measuring spiked aliquots of the BIR-1 and BHVO-2 geostandards. The results of 7 analyses of BHVO-2 yielded an average  $^{176}\text{Hf}/^{177}\text{Hf}$  value of  $0.283094 \pm 0.000030$  (2 S.D.) and a  $^{176}\text{Lu}/^{177}\text{Hf}$  ratio of  $0.0086 \pm 0.0001$  (2 S.D.). Analyses of the BIR-1 geostandard ( $N=5$ ) yielded  $^{176}\text{Hf}/^{177}\text{Hf}=0.283256 \pm 0.000070$  and  $^{176}\text{Lu}/^{177}\text{Hf}=0.0584 \pm 0.0022$ . The  $^{176}\text{Hf}/^{177}\text{Hf}$  values obtained for both geostandards are within error of those previously reported (e.g. Weis et al., 2007, and references therein), confirming the accuracy of the spike corrected ratios.

## 5. Results

The  $^{176}\text{Lu}$ - $^{176}\text{Hf}$  results from this study and previous  $^{146,147}\text{Sm}$ - $^{142,143}\text{Nd}$  data for mafic and ultramafic rocks from the Saglek block are presented in Table 3 and summarized in Figure 5. By convention,  $^{176}\text{Hf}/^{177}\text{Hf}$  and  $^{143}\text{Nd}/^{144}\text{Nd}$  isotopic ratios are expressed by their relative deviation in parts per 10,000 from the chondritic value (Bouvier et al., 2008) at the time of interest, using the conventional epsilon ( $\epsilon$ ) notation. Variations of  $^{142}\text{Nd}/^{144}\text{Nd}$ , noted  $\mu^{142}\text{Nd}$ , are expressed by their

deviation (in ppm) from the JNdi standard, which is considered representative of the Bulk Silicate Earth.

Measured  $^{176}\text{Hf}/^{177}\text{Hf}$  values range from 0.281785 to 0.283040 among the Mesoarchean samples and from 0.281152 to 0.287879 among the Eoarchean samples (Table 3). Regressions of these values as a function of  $^{176}\text{Lu}/^{177}\text{Hf}$  were calculated using the Isoplot/Ex software (version 4.15; Ludwig, 2012), and initial  $^{176}\text{Hf}/^{177}\text{Hf}$  values were calculated from the whole-rock errorchrons using the method of Fletcher and Rosman (1982). Uncertainties on  $^{176}\text{Hf}/^{177}\text{Hf}$  values are taken to  $\pm 35$  ppm and are based on the 2 S.D. variation of repeated analyses of the JMC-475 Hf standard. Where two or more analyses were available for an individual sample, the mean value was used. Age calculations were performed using a  $^{176}\text{Lu}$  decay constant of  $1.867 \cdot 10^{-11}$  (Scherer et al., 2001; Söderlund et al., 2004). Errors on ages and initial  $^{176}\text{Hf}/^{177}\text{Hf}$  calculated by linear regression are quoted as 2 S.D. The results (Fig. 2) confirm the presence of two mafic/ultramafic suites in the Saglek block, as previously inferred from their  $^{142,143}\text{Nd}$  systematics (Morino et al 2017). Regression of the Mesoarchean group, without  $^{142}\text{Nd}$  anomaly, yields an age of  $3023 \pm 390$  Ma (MSWD=84) with an initial  $^{176}\text{Hf}/^{177}\text{Hf} = 0.280825 \pm 0.000071$ , corresponding to  $\epsilon^{176}\text{Hf}_{(3,0)} = -0.31 \pm 2.5$  (Fig. 2). This age is consistent with the  $^{147}\text{Sm}$ - $^{143}\text{Nd}$  age of  $3365 \pm 100$  Ma obtained by Morino et al (2017) but remains poorly defined owing to limited spread in Lu/Hf among the analyzed samples. The slope of the regression line is also largely determined by sample LA11-14, which may have been affected by crustal contamination (Section 3). Despite the large uncertainty associated with the whole-rock regression, the near-chondritic  $\epsilon^{176}\text{Hf}$  inferred for the Mesoarchean suite appears robust, showing only weak dependence on actual emplacement age. Initial  $\epsilon^{176}\text{Hf}$  values for individual samples based on the more precisely defined  $^{147}\text{Sm}$ - $^{143}\text{Nd}$  age remain within error of the chondritic value, with a mean  $\epsilon^{176}\text{Hf}_{(3,36)} = 1.4 \pm 1.7$  (2 S.E., Standard Error). Considered together with the previously determined  $\epsilon^{143}\text{Nd}_{(3,36)}$  of  $0.4 \pm 0.4$  (Morino et al 2017), this result suggests derivation of the Mesoarchean ultramafic suite from an undepleted mantle source with near-chondritic Lu/Hf and Sm/Nd.

Regression of Nulliak mafic and ultramafic samples carrying a positive  $^{142}\text{Nd}$  anomaly yields a slope corresponding to an age of  $3794 \pm 130$  Ma (MSWD=142) with an initial  $^{176}\text{Hf}/^{177}\text{Hf}$

=0.280461±0.000064,  $\epsilon^{176}\text{Hf}_{(3.79)}=5.1\pm2.3$  (Fig. 5). This age remains unchanged when considering only  
 ultramafic samples in the regression ( $T=3766\pm140$  Ma; MSWD=118;  $^{176}\text{Hf}/^{177}\text{Hf}$   
 =0.280504±0.000072,  $\epsilon^{176}\text{Hf}_{(3.77)}=6.0\pm2.5$ ). Discarding two samples with high Ce/Yb, possibly  
 reflecting crustal assimilation (section 3), also yields a similar age and initial  $^{176}\text{Hf}/^{177}\text{Hf}$  ( $T=3818\pm170$   
 Ma,  $^{176}\text{Hf}/^{177}\text{Hf}=0.280466\pm0.000080$ , MSWD=95,  $\epsilon^{176}\text{Hf}_{(3.82)}=5.8\pm2.9$ ). All regression lines thus yield  
 $^{176}\text{Lu}$ - $^{176}\text{Hf}$  ages consistent with the previously determined  $^{147}\text{Sm}$ - $^{143}\text{Nd}$  age of  $3782\pm93$  Ma (Morino et  
 al., 2017). Both the  $^{147}\text{Sm}$ - $^{143}\text{Nd}$  and  $^{176}\text{Lu}$ - $^{176}\text{Hf}$  ages are also indistinguishable from the U-Pb zircon  
 date of  $3776\pm8$  Ma obtained by Schiøtte (1989) from a metavolcanic unit of the Nulliak assemblage  
 situated on Bluebell island (Saglek Bay). This excellent agreement argues that the Lu-Hf dates have  
 geologic significance despite the elevated MSWD values of the regressions. We thus interpret the  
 initial  $^{176}\text{Hf}/^{177}\text{Hf}$  of the ultramafic rocks ( $0.280504\pm0.000072$ ;  $\epsilon^{176}\text{Hf}_{(3.77)}=6.0\pm2.5$ ) to reflect  
 derivation of the Nulliak ultramafic suite from a mantle source with super-chondritic Lu/Hf.

## 6. Discussion

### 5.1. Lu/Hf and Sm/Nd composition of the Early Depleted Mantle

The knowledge of  $^{142,143}\text{Nd}$  and  $^{176}\text{Hf}$  signatures of Nulliak ultramafic rocks offers the opportunity  
 to precisely determine the time-integrated  $^{147}\text{Sm}/^{144}\text{Nd}$  and  $^{176}\text{Lu}/^{177}\text{Hf}$  of the EDM. Using coupled  
 $^{146,147}\text{Sm}$ - $^{142,143}\text{Nd}$  systematics, Morino et al (2017) estimated the former to be  $0.211\pm0.007$ , with a  
 corresponding model age of differentiation of 4.4 Ga. Following this simple approach, the  $^{176}\text{Lu}/^{177}\text{Hf}$   
 of the Nulliak source is calculated using a two-stage evolution model with an instantaneous  
 differentiation event at  $T_d=4.4$  Ga. The mantle is assumed to evolve with a chondritic Lu/Hf prior to  
 this date and a fractionated Lu/Hf afterwards. This differentiation event creates the early depleted  
 mantle (EDM) considered here as the Nulliak source. Evolution of the  $^{176}\text{Lu}$ - $^{177}\text{Hf}$  system in this two-  
 stage model is described by the following equation:

$$\left( \frac{^{176}\text{Hf}}{^{177}\text{Hf}} \right)_{T_e}^{\text{EDM}} = \left( \frac{^{176}\text{Hf}}{^{177}\text{Hf}} \right)_{T_p}^{\text{CHUR}} + \left( \frac{^{176}\text{Lu}}{^{177}\text{Hf}} \right)_{T_p}^{\text{CHUR}} \left[ 1 - e^{\lambda_{176} T_e} \right] + \left( \frac{^{176}\text{Lu}}{^{177}\text{Hf}} \right)_{T_p}^{\text{EDM}} \left[ e^{\lambda_{176} T_d} - e^{\lambda_{176} T_e} \right] \quad (1)$$

Where  $\lambda_{176}$  is the  $^{176}\text{Lu}$  decay constant ( $1.867 \cdot 10^{-11}$ ; Scherer et al., 2001; Söderlund et al., 2004),  $(^{176}\text{Lu}/^{177}\text{Hf})_{\text{CHUR}}=0.0336$  and  $(^{176}\text{Hf}/^{177}\text{Hf})_{\text{CHUR}}=0.282785$  at  $T_p$  is the present-day composition of the Chondritic Uniform Reservoir (Bouvier et al, 2008),  $T_d$  is the differentiation age of the EDM obtained from coupled  $^{146,147}\text{Sm}$ - $^{142,143}\text{Nd}$  systematics (Morino et al 2017) and  $T_e$  is the time at which the parental melts of the Nulliak suite were extracted from the EDM. Application of Equation (1) with  $T_e=3.77$  Ga and  $(^{176}\text{Hf}/^{177}\text{Hf})_{T_e}=0.280504\pm0.000072$  yields a time-integrated  $(^{176}\text{Lu}/^{177}\text{Hf})_{\text{EDM}}$  of  $0.047\pm0.005$  for a corresponding  $(^{147}\text{Sm}/^{144}\text{Nd})_{\text{EDM}}$  of  $0.211\pm0.007$ . By comparison, the time-integrated  $^{176}\text{Lu}/^{177}\text{Hf}$  and  $^{147}\text{Sm}/^{144}\text{Nd}$  values of the present-day depleted mantle are estimated to be  $0.042$ - $0.047$  and  $0.22$ - $0.24$ , respectively, assuming a mean age of  $1.8$ - $2.8$  Ga for mantle depletion from a chondritic source (Salters and Stracke, 2004) and chondritic  $^{176}\text{Lu}/^{177}\text{Hf}$  and  $^{147}\text{Sm}/^{144}\text{Nd}$  values of  $0.0336$  and  $0.1960$  (Bouvier et al, 2008). The EDM and the MORB source thus exhibit similar Lu/Hf but differ in that the EDM was characterized by a less fractionated LREE pattern.

The  $^{147}\text{Sm}/^{144}\text{Nd}$  and  $^{176}\text{Lu}/^{177}\text{Hf}$  obtained for the sources of the Eo- and Mesoarchean ultramafic suites of the Saglek block are summarized in Figure 6, together with those obtained for the sources of Isua amphibolites (Hoffmann et al., 2010; Rizo et al., 2012) and several Mesoarchean komatiites of the Kaapvaal craton (Puchtel et al., 2013; Hoffmann and Wilson, 2016; Puchtel et al., 2016). The  $(^{176}\text{Lu}/^{177}\text{Hf})_{\text{EDM}}$  inferred from Nulliak ultramafic rocks is similar to that estimated for the source of boninite-like metabasalts of the ISB (Hoffmann et al., 2010) but differs markedly from the slightly subchondritic value inferred from ISB meta-tholeiites (Rizo et al., 2012). This observation could imply a heterogeneous composition of the EDM with respect to Hf isotopes, or, alternatively, decoupling of  $^{176}\text{Lu}$ - $^{176}\text{Hf}$  and  $^{147}\text{Sm}$ - $^{143}\text{Nd}$  systematics in the source of ISB meta-tholeiites, possibly related to the recycling of detrital components (Hoffmann et al., 2010; Hoffmann et al., 2011). In any case, our results show that the slightly subchondritic Lu/Hf inferred for the source of some ISB meta-tholeiites is not fully representative of the EDM. Rather, the concordant results obtained from Nulliak ultramafic rocks and ISB boninite-like metabasalts indicate that their positive  $^{142}\text{Nd}$  anomalies were produced in a mantle reservoir having superchondritic Sm/Nd and Lu/Hf.

Collectively, Eo- and Mesoarchean komatiites of the Saglek block and Kaapvaal craton define an  $\epsilon^{176}\text{Hf}$ - $\epsilon^{143}\text{Nd}$  array with a slope of  $\approx 4$  that differs significantly from the present-day mantle array ( $\epsilon^{176}\text{Hf} \approx 1.6 \times \epsilon^{143}\text{Nd}$ , Chauvel et al., 2008). This observation demonstrates that mantle differentiation processes in the early Earth differed markedly from those that operated throughout much of Earth's history to produce the present-day depleted mantle. A simple interpretation could be that both the modern Hf-Nd array and the komatiite array illustrated in Figure 6 formed as a result of melt extraction, but that the latter reflects deeper melting in the early Earth. Partial melting in a hotter mantle would involve larger extents of fractionation in the garnet stability field, which in turn could produce a residual mantle with elevated Lu/Hf. It is important to recognize, however, that the high Lu/Hf characterizing the EDM is not representative of the Archean depleted mantle, but appears to represent a single component in the source of Eo- and Mesoarchean komatiites. By contrast, protoliths of Archean TTGs (tonalite-trondhjemite-granodiorite) consistently sampled a mantle reservoir with only slightly superchondritic Lu/Hf (0.032-0.038, Guitreau et al., 2012). The Hf-Nd signature of the EDM also differs from that observed in Neoarchean komatiites, which plot on the present-day mantle array (Blichert-Toft and Puchtel, 2010; Puchtel et al., 2016). This observation suggests that the composition of the depleted reservoir sampled by komatiite magmatism evolved with time, in response to changes in global mantle-crust differentiation processes. The Hf-Nd signature of Neoarchean komatiites is consistent with their extraction from a mantle reservoir depleted by formation of the continental crust, while the Nulliak Hf-Nd signature likely records trace element fractionation associated with primordial mantle differentiation during the final stage of terrestrial accretion. In the following sections, we further evaluate this hypothesis in the framework of a simplified model of magma ocean crystallization. Our goal is to constrain the depth at which differentiation of the EDM reservoir occurred and to explore the possible geodynamic implications.

## 5.2. The magma ocean crystallization model

Two scenarios for solidification of the terrestrial magma ocean are considered in the following sections. In Model 1, we investigate Lu/Hf and Sm/Nd fractionation at lower mantle pressures, in the presence of an assemblage composed of ferropericlase, bridgmanite and Ca-perovskite. Following



Elkins-Tanton (2008), we assume that the magma ocean reached a depth of 2000 km. Crystallization most likely started from the bottom and proceeded upward because the thermal adiabat crosses the liquidus curve at the base of the mantle (e.g. Solomatov and Louis, 2007). Trace element partition coefficients in perovskite estimated at 23-25 GPa are assumed to remain valid throughout the lower mantle, which is treated as a single homogeneous reservoir. Model 2 considers the sequential crystallization of a shallow magma ocean from the transition zone to the surface (Caro et al., 2005). In this model, Earth's upper mantle is subdivided into 6 layers (22-18 GPa, 18-15 GPa, 15-12 GPa, 12-7 GPa, 7-4.5 GPa, 4.5-2 GPa) to account for changes in mineralogy and garnet/melt partition coefficients. Crystallization is assumed to proceed from the bottom up, and the residual liquid remaining after the full crystallization of each layer is used as the starting liquid composition for the overlying layer (Caro et al., 2005). The impact of trapped liquid on Lu/Hf and Sm/Nd fractionation will be also considered. The mineral proportions for each layer, derived from Elkins-Tanton (2008) and Irifune (1994), are consistent with a pyrolitic mantle composition (Fig 7). For the sake of simplicity, it is assumed that all mineral phases grow synchronously, that the solid phases equilibrate with all of the remaining liquid during the growth of each layer (ie, that the liquid composition is homogeneous at each point in time), and that the modal proportions remain constant during crystallization within each of the layers. We acknowledge that these assumptions are unlikely to be valid throughout the entire crystallization sequence. Nevertheless, this simplified model provides an adequate framework to investigate the relationships between Lu/Hf and Sm/Nd fractionation expected to occur at various depths in the terrestrial magma ocean.

In both models, we assume a homogeneous initial melt with a pyrolitic composition and chondritic Lu/Hf and Sm/Nd (McDonough and Sun, 1995). During crystallization, elemental fractionation is controlled by the partition coefficient  $D$  of the bulk mineral assemblage relative to the melt, which is calculated according to the following equation;

$$D = \sum y_j K_{d_j} \quad (2)$$

Where  $j$  represents the mineral,  $y$  its proportion in the mineralogical assemblage and  $K_d$  the partition coefficient between the mineral and the melt. The chosen partition coefficients for this model are compiled from the literature and reported in Table 4 (Salters and Longhi, 1999; Draper et al., 2003; Corgne, 2004; Corgne et al., 2004; Corgne and Wood, 2004; Corgne et al., 2012). Whenever possible, partition coefficients were selected from experiments using pyrolitic or chondritic starting compositions at the appropriate pressure range (i.e. 23-25 GPa for bridgmanite, ferropericlase and Ca-perovskite, 15-25 GPa for majorite, 2.8-9 GPa for garnet). When high pressure data were unavailable (clinopyroxene, orthopyroxene), partition coefficients at 2.8 GPa from Salters and Longhi (1999) were used. At lower mantle pressures, Lu/Hf and Sm/Nd fractionation are controlled by bridgmanite and Ca-perovskite, whereas at upper mantle pressure, garnet and clinopyroxene have the strongest influence. All elements of interest are highly incompatible in olivine (e.g. Salters and Longhi, 1999). Partition coefficients in olivine and its high pressure polymorphs were therefore assumed to be zero for all elements of interest. It is assumed that within each layer, partition coefficients do not vary with pressure, composition or temperature.

The evolution of the of bulk partition coefficients (noted  $D_{Lu}/D_{Hf}$  and  $D_{Sm}/D_{Nd}$ ) across the mantle illustrates the strong pressure dependence of Lu/Hf fractionation (Fig. 7); As  $P$  increases,  $D_{Lu}$  in the bulk mineral assemblage decreases from 7 at 3 GPa to 1 at >15 GPa, while  $D_{Hf}$  remains roughly constant, at ca. 0.03-0.07. The largest Lu/Hf fractionation is thus expected to occur at pressures between 2 and 5 GPa (Pressures less than ~2 GPa are not considered because garnet is not stable.) At lower mantle pressures, Hf is expected to become more compatible than Lu ( $D_{Lu}/D_{Hf}<1$ ), while  $D_{Sm}/D_{Nd}$  remains above 1 throughout the upper and lower mantle.

The extent of chemical differentiation in a magma ocean depends on whether melt can segregate from the solid phase during crystallization. This in turn depends on several factors (Solomatov and Louis, 2007), such as the crystal size (which controls the sedimentation rate), the cooling rate, the rate of melt percolation and the density contrast between melt and solid. Solomatov and Louis (2007) estimated that solidification of the lower mantle proceeded rapidly ( $10^3$  yr), effectively hampering chemical differentiation, while the upper mantle would have crystallized on  $10^7$ -

476  $10^8$  yr timescales compatible with some degree of melt extraction. In any case, rapid progression of the  
 477 solidification front is likely to trap a substantial amount of liquid in the partially molten regions,  
 478 ultimately resulting in subdued chemical fractionation compared to that expected from a pure  
 479 cumulate. To account for this effect, the model includes a trapped liquid component, modelled as a  
 480 mineral phase with partition coefficients of 1 for all elements of interest. It is assumed that the fraction  
 481 of trapped liquid is the same in the different layers.

482 Chemical differentiation in the magma ocean may have proceeded through either batch or  
 483 fractional crystallization. During the early stages of solidification, turbulent convection likely favored  
 484 batch crystallization, while fractional crystallization may have been the predominant mechanism at  
 485 small (<20%) fractions of residual melt (Snyder et al., 1992; Borg and Draper, 2003; Debaille et al.,  
 486 2008). As the transition from batch to fractional processes is poorly constrained, the effects of these  
 487 two modes of crystallization on Lu/Hf and Sm/Nd fractionation were investigated throughout the  
 488 entire crystallization sequence. The results are very similar for batch and fractional crystallization (see  
 489 online appendix) so these processes are not discussed separately in the following sections.

490 Elemental concentrations were calculated from the following equations, for batch (Eq. 3-4)  
 491 and fractional (Eq. 5-6) crystallization:

$$492 \quad \begin{cases} \left( \frac{C_i^l}{C_i^0} \right) = \frac{1}{DX + (1-X)} \\ \left( \frac{C_i^s}{C_i^0} \right) = \frac{D}{DX + (1-X)} \end{cases} \quad (3-4)$$

$$493 \quad \begin{cases} \left( \frac{C_i^l}{C_i^0} \right) = (1-X)^{D-1} \\ \left( \frac{C_i^s}{C_i^0} \right) = \frac{1-(1-X)^D}{X} \end{cases} \quad (5-6)$$

494 Where  $C_i^l$  is the concentration of element  $i$  remaining in the liquid,  $C_i^s$  is the concentration of element  
 495  $i$  in the cumulate and  $C_i^0$  is the initial concentration in the melt,  $X$  corresponds to the extent of

crystallization within a given layer and  $D$  is the partition coefficient of the crystallizing mineralogical assemblage. Sequential crystallization of the upper mantle is modelled according to the following procedure. The deepest reservoir (22-18 GPa), here composed of majorite and olivine, crystallizes from a pyrolytic melt until its total solidification, and the residual melt is taken as the starting composition for the next step of crystallization. This calculation is then repeated for the next 5 layers until the upper mantle reaches 93% solidification. The composition of the final liquid thus corresponds to the last 7% of residual melt, which is equivalent to 3% of the mass of the BSE.

### 5.3. Lu/Hf and Sm/Nd fractionation in the terrestrial magma ocean

Results of both models are presented in Figure 8, for the batch crystallization case. Results corresponding to the fractional crystallization case are provided in supplementary material. Similar to previous studies, Model 1 predicts a strong decoupling of Lu/Hf and Sm/Nd at lower mantle pressures (Caro et al., 2005, Rizo et al., 2011). Depending on the relative proportions of bridgmanite and Ca-perovskite, batch and fractional crystallization yield cumulates with  $^{176}\text{Lu}/^{177}\text{Hf}$  ranging from 0.028 to 0.035 and  $^{147}\text{Sm}/^{144}\text{Nd}$  ranging from 0.20 to 0.26 (compared to the chondritic values of 0.0336 and 0.196, respectively) after complete crystallization of the lower mantle, representing ~62% of the total volume of the magma ocean. Crystallization of the lower mantle in roughly modal proportions, (7% Ca-perovskite; 75% bridgmanite, 18% ferropericlasite) would produce a cumulate with a near-chondritic Lu/Hf (0.034) but superchondritic Sm/Nd, leading with time to slightly positive  $\varepsilon^{176}\text{Hf}$  (~0.2 at  $T=3.75$  Ga) and positive  $\varepsilon^{142,143}\text{Nd}$  (Fig. 8A). The decoupling of Sm/Nd and Lu/Hf fractionation induced by crystallization of a perovskitic reservoir is consistent with the signature reported by Rizo et al. (2011) for Isua metatholeiites, but cannot explain the signature of the Nulliak source ( $^{176}\text{Lu}/^{177}\text{Hf}=0.047$ ,  $^{147}\text{Sm}/^{144}\text{Nd}=0.211$ ), and, by extension, the slope of the Hf-Nd komatiite array (Fig. 6).

For the upper mantle model (Model 2), all cumulates generated from the transition zone to the surface exhibit highly fractionated Lu/Hf and Sm/Nd, predominantly induced by the garnet component

(Fig. 8B). The  $^{176}\text{Lu}/^{177}\text{Hf}$  and  $^{147}\text{Sm}/^{144}\text{Nd}$  ratios in upper mantle cumulates range from 0.10 to 0.14 and from 0.30 to 0.52, respectively. Crystallization of a shallow magma ocean is therefore expected to produce a depleted upper mantle with positive  $\epsilon^{176}\text{Hf}$  and  $\epsilon^{142,143}\text{Nd}$ , generally consistent with the signature inferred for the Nulliak source. However, while crystallization at upper mantle pressures can explain the direction of displacement of the calculated  $(\text{Lu}/\text{Hf})_{\text{EDM}}$  and  $(\text{Sm}/\text{Nd})_{\text{EDM}}$  relative to a chondritic composition, the model produces cumulates with Sm/Nd and Lu/Hf markedly higher than those estimated for the Nulliak source. It follows that crystallization of a shallow magma ocean cannot reproduce the composition of the EDM unless chemical fractionation was buffered by trapping of liquid during solidification.

Figure 9 shows the composition of magma ocean cumulates at the different pressure ranges considered in Model 2, assuming a fraction of trapped liquid between 5% and 30%. The results show little dependence upon pressure or mineralogical assemblage and the produced trends all fit the Nulliak source composition within the calculated uncertainties. Nevertheless, the best fit to the Nulliak composition is obtained for a depth range of 60-400 km, and a fraction of trapped liquid of 5-15%. Radiogenic decay in these reservoirs would translate into an approximately 4:1 relationship between  $\epsilon^{176}\text{Hf}$  and  $\epsilon^{143}\text{Nd}$  consistent with the initial ratios deduced from the Nulliak Sm-Nd and Lu-Hf errorchrons. We thus interpret the  $^{176}\text{Hf}$ - $^{142,143}\text{Nd}$  composition of the Nulliak ultramafic rocks to reflect differentiation of the EDM at relatively low pressure in the upper mantle. Our results also show that Eo- and Mesoarchean komatiites, while often viewed as originating from the deep mantle, carry  $^{176}\text{Hf}$ - $^{143}\text{Nd}$  signatures consistent with prior differentiation of their source in the garnet stability field (Fig. 6).

#### *5.4. Geodynamic evolution of the EDM*

In absence of a clear perovskite signature, the interpretation that the EDM formed by magma ocean crystallization rather than by partial melting of a solidified mantle relies solely on chronological constraints. The synchronicity of the  $^{146,147}\text{Sm}$ - $^{142,143}\text{Nd}$  model age for differentiation of the silicate

Earth with the Pb-Pb age thought to reflect impact-provoked Pb loss (Connelly and Bizzarro, 2016) suggests that the EDM was produced near the end of terrestrial accretion, most likely as a result of extensive melting triggered by the Moon-forming impact. However, whether the EDM represents magma ocean cumulates or the residue of post-crystallization melting remains uncertain. Regardless of the exact mechanism by which the EDM formed, our results indicate that differentiation must have taken place at relatively low pressure within the garnet stability field. This shallow depleted reservoir must have remained at least partially isolated from the convective system, so as to account for the presence of positive  $^{142}\text{Nd}$  anomalies in Neoarchean lavas of the Abitibi belt (Debaille et al, 2013). Long-term preservation of primordial mantle domains could imply inefficient convective stirring in the early Earth, perhaps due to the presence of a stagnant-lid regime (Debaille et al., 2013). However, several lines of evidence suggest that ancient mantle domains remained isolated on a billion year timescale near the core-mantle boundary, and are still sampled by modern plume magmatism (Mukhopadhyay, 2012; Caracausi et al., 2016; Rizo et al., 2016; Mundl et al., 2017; Peters et al., 2018). In this regard, an important observation is that while the EDM (or mantle domains with similar Lu/Hf and Sm/Nd) contributed to the source of Eo- and some MesoArchean komatiites, as shown by the correlation between the Lu/Hf vs. Sm/Nd values of their sources (Figure 6), this reservoir was not commonly tapped by magmatism involved in Archean crustal growth (Guitreau et al., 2012).

Magma ocean overturn provides a scenario which can potentially account for these observations. Overturn would occur during or shortly after solidification, reorganizing the stratification according to cumulate density (Elkins-Tanton et al., 2003; Elkins-Tanton et al., 2005; Elkins-Tanton, 2008; Brown et al., 2014). This would result in the sinking of shallow and dense cumulates to depths near the core-mantle boundary, which would trigger a return flow of deep undifferentiated material into the upper mantle. The storage of dense upper mantle cumulates at the core mantle boundary would favor their long-term preservation, consistent with the apparent closed system evolution of the EDM, while the transfer of deep undifferentiated material into the upper mantle may account for the near-chondritic Lu/Hf ratio characterizing the mantle source of the protoliths of Archean TTGs (Guitreau et al., 2012). Alternatively, it is entirely plausible that chemical

differentiation in the magma ocean remained marginal until the ultimate stage of solidification, hampered by inefficient crystal settling and rapid cooling of the mantle compared to the rate of melt percolation. Effective chemical fractionation may then only be possible in the shallowest part of the upper mantle (Solomatov and Louis, 2007). In this case, the shallow depleted reservoir would be chemically buoyant, favoring its long-term preservation as part of a long-lived stagnant lid (O'Neill and Debaille, 2014; Caro et al., 2017). Recycling of this primordial lithosphere would then provide a means of transferring both enriched and depleted material into the deep mantle where they may have contributed in various proportions to plume-related magmatism.

## 7. Conclusions

Because of its sensitivity to pressure, the  $^{176}\text{Lu}$ - $^{176}\text{Hf}$  system provides a means of constraining the depths of differentiation of the mantle sources of volcanic rocks. This approach was undertaken on mafic and ultramafic rocks of the Saglek block (northern Labrador, Canada) in order to assess the composition and differentiation mechanism of mantle domains carrying positive  $^{142}\text{Nd}$  anomalies. The results of this study can be summarized as follows:

1) The two suites of mafic and ultramafic rocks of the Saglek Block, identified by Morino et al. (2017) on the basis of their  $^{142}\text{Nd}$  compositions, yielded  $^{176}\text{Lu}$ - $^{176}\text{Hf}$  whole-rock errorochrons with ages consistent with those previously determined by  $^{147}\text{Sm}$ - $^{143}\text{Nd}$  dating. This finding confirms the existence of the two-distinct series, the Eoarchean Nulliak suite with a  $^{176}\text{Lu}$ - $^{176}\text{Hf}$  age of  $3766\pm140$  Ma ( $3782\pm93$  Ma by  $^{147}\text{Sm}$ - $^{143}\text{Nd}$ ), and a Mesoarchean suite, dated at  $3023\pm390$  Ma (compared to  $3365\pm100$  Ma by  $^{147}\text{Sm}$ - $^{143}\text{Nd}$ ). These age constraints are consistent with U-Pb dating of magmatic and detrital zircons from the Nulliak and Upernavik formations (Schiotte, 1989; Schiotte et al, 1989, 1992) and with the  $^{187}\text{Re}$ - $^{187}\text{Os}$  study from Ishikawa et al. (2017), who reported minimum model ages ( $T_{\text{RD}}$ ) of 3.4-3.6 Ga and 2.8-3.3 Ga in two ultramafic suites of the Saglek block.

2) The model age ( $4.40\pm0.03$  Ga) obtained by Morino et al. (2017) for the formation of the EDM was used to calculate the time-integrated Lu/Hf source ratios for each of the suites, yielding  $^{176}\text{Lu}/^{177}\text{Hf}$  ratios of 0.047 and 0.033 for the Eoarchean and Mesoarchean mantle sources respectively. The

superchondritic  $^{176}\text{Lu}/^{177}\text{Hf}$  of the Nulliak source is coupled with a superchondritic  $^{147}\text{Sm}/^{144}\text{Nd}$  ( $\approx 0.21$ ). In order to investigate the origin of this coupled signature, we developed a simple model of magma ocean crystallization. Results show that garnet played a critical role in the fractionation of Lu/Hf and Sm/Nd of the Nulliak mantle source. More specifically, our modeling results imply that the isotopic signature of the Nulliak suite was generated by crystallization of its parent mantle reservoir above the transition zone, in a depth range of 400 to 60 km. Substantial quantities of trapped liquid are required in the cumulate pile, but the proportions cannot be estimated unambiguously given the simplifying assumptions made in the model.

3) When the parameters for the Nulliak source as well as for the mantle sources of other Eo- and Mesoarchean komatiites are plotted in a diagram of Sm/Nd versus Lu/Hf, a well-defined trend is observed, suggesting a single formation mechanism for the sources of all of these komatiites. This trend differs from the Hf-Nd mantle array defined by modern basalts, having more radiogenic Hf isotopic compositions for a given Nd isotopic ratio. This observation may be consistent with our interpretation that the source of Eo- and Mesoarchean komatiites formed by melting or crystallization processes involving garnet at depths of 400 to 60 km. This contrasts with the likely origin of the modern Hf-Nd array, which would involve melt extraction at mostly shallower depths, including a large component in the spinel facies in the absence of garnet.

4) The conclusion that the differentiation of Eo- and Mesoarchean komatiite sources occurred in the upper mantle could appear surprising considering that these magmas are thought to be derived from the deep mantle. This suggests that a mantle overturn mechanism brought the komatiite source reservoirs, which differentiated in the garnet stability field, down into the deep mantle, where they were effectively isolated for hundreds of millions of years. This deep mantle source was then sporadically sampled by plume mechanisms.

#### Acknowledgements:

We acknowledge the very constructive reviews by Erik Scherer, Igor Puchtel, and an anonymous reviewer as well as AE James Day for his efficient editorial handling. A. Schumacher and D. Cividini are thanked for providing assistance



627 on the ICP-MS work. We thank Béatrice Luais and Albert Galy for technical discussions during the development  
628 stages of this work. We also thank Emilie Thomassot and all members of the Saglek Block expedition as well as those  
629 who participated in its organization. We are grateful to the financial support from Agence Nationale de la Recherche  
630 (grant ANR-11-JS-0012) and the Région Lorraine, through a doctoral fellowship allocated to P.M.

631

632

633

### Figure captions

634 **Fig. 1.** Geological location and simplified geological map of the Hebron fjord - Saglek fjord region of  
 635 the Saglek block, showing the location of the main sampling sites (from Morino et al., 2017 Modified  
 636 from Ryan and Martineau (2012)). Large ( $\approx 100$ -1000 m) enclaves composed of both mafic and  
 637 ultramafic rocks are referred to as units A, B and C. The dotted rectangle indicates the general area  
 638 where smaller (meter-sized) enclaves were collected. Correlated sample numbers and GPS coordinates  
 639 are provided in Morino et al. (2017).

640 **Fig. 2.** (A-H) Selected trace elements versus Zr in ultramafic rocks of the Eo- and Mesoarchean suites  
 641 of the Saglek block. Full symbols represent samples with  $(\text{Ce/Yb})_N$  within the range of  
 642 uncontaminated komatiites (Cf. Fig. 3). Open symbols represent samples with anomalous  $(\text{Ce/Yb})_N$ ,  
 643 possibly reflecting crustal contamination.

644 **Fig. 3.** (A-C) Selected trace element ratios versus  $(\text{Ce/Yb})_N$  in ultramafic rocks from the Saglek block.  
 645 Komatiites of the Barberton and Abitibi greenstone belts, and Gorgona Island are shown for  
 646 comparison. Komatiite data are compiled from the GEOROC database ([http://georoc.mpch-](http://georoc.mpch-mainz.gwdg.de)  
 647 [mainz.gwdg.de](http://georoc.mpch-mainz.gwdg.de)). Average Archean TTGs (tonalite-trondjemite-granodiorite) have  $(\text{Ce/Yb})_N \approx 15$ ,  
 648  $(\text{Th/La})_N \approx 2$ ,  $(\text{Nb/La})_N \approx 0.25$ ,  $(\text{Sm/Nd})_N \approx 0.5$  (Condie, 1993). Note that three samples from the  
 649 Eoarchean group and one from the Mesoarchean group have Th concentrations below the detection  
 650 limit of 0.06 ppm. The corresponding datapoints (marked by descending arrows in panel B) represent  
 651 maximum  $(\text{Th/La})_N$  values.

652 **Fig. 4.**  $(\text{Lu/Hf})_N$  versus  $\text{Al}_2\text{O}_3/\text{TiO}_2$  in ultramafic rocks of the Saglek block. Data for Barberton,  
 653 Abitibi and Gorgona komatiites are compiled from the GEOROC database ([http://georoc.mpch-](http://georoc.mpch-mainz.gwdg.de)  
 654 [mainz.gwdg.de](http://georoc.mpch-mainz.gwdg.de)).

655 **Fig. 5.** (A-B) Lu-Hf isochron diagrams for mafic/ultramafic enclaves of the Saglek Block. The  
 656 regression for the panel A includes rocks that were affiliated with a Mesoarchean event by Morino et  
 657 al. (2017). The regression in panel B includes samples previously defined as Eoarchean. (C-D)  $^{147}\text{Sm}$ -  
 658  $^{143}\text{Nd}$  isochron diagrams for mafic/ultramafic enclaves of the Saglek block from Morino et al. (2017).  
 659 Uncertainties on ages and initial ratios are 2 S.D. Regressions were performed using Isoplot/Ex  
 660 version 4.15 (Ludwig, 2012), assuming a typical uncertainty of 0.5% on  $^{147}\text{Sm}/^{144}\text{Nd}$  and  $^{176}\text{Lu}/^{177}\text{Hf}$ .

661

662 **Fig. 6.**  $^{176}\text{Lu}/^{177}\text{Hf}$  versus  $^{147}\text{Sm}/^{144}\text{Nd}$  of the sources of the Saglek ultramafic suites compared to the  
 663 sources of Mesoarchean komatiites and Isua mafic rocks. The grey field represents the modern  
 664 terrestrial array (Chauvel et al., 2008).  $^{147}\text{Sm}/^{144}\text{Nd}$  and  $^{176}\text{Lu}/^{177}\text{Hf}$  source ratios are calculated

according to Eq. (1), assuming a differentiation event at 4.4 Ga and considering 2 S.D. uncertainties on initial  $\varepsilon^{176}\text{Hf}$  values from the Isoplot regression. For nearly all localities, the parameters of the mantle source were calculated using the initial ratios of the corresponding isochrons. The sole exception concerns the Isua boninites, for which the mean  $^{147}\text{Sm}/^{144}\text{Nd}$  and  $^{176}\text{Lu}/^{177}\text{Hf}$  values were determined from the mantle source parameters calculated individually for each sample; the uncertainties shown represent the 2 S.D. variations of these mean values. Note that model ages of differentiation for the mantle sources of Kaapvaal komatiites (i.e.  $T_d$  in Equation (1)) cannot be inferred from  $^{146,147}\text{Sm}$ - $^{142,143}\text{Nd}$ , either due to absence of  $^{142}\text{Nd}$  data or due to an apparent decoupling of the  $^{146}\text{Sm}$ - $^{142}\text{Nd}$  and  $^{147}\text{Sm}$ - $^{143}\text{Nd}$  systems (Puchtel et al., 2016). Accordingly, the time-integrated Lu/Hf and Sm/Nd values of their mantle sources cannot be estimated with as much confidence as for the Isua and Nulliak sources and should be considered first-order estimates. The blue and yellow envelopes represent the calculated compositions of magma ocean cumulates predicted to crystallize at lower and upper mantle pressures, respectively (See Section 5 and Figures 8-9).

**Fig. 7. A.** Modal compositions of mineral assemblages considered for models 1 and 2 of crystallization of a terrestrial magma ocean (Opx: Orthopyroxene, Cpx: Clinopyroxene; Ca-Pv: Ca-perovskite, Bg: Bridgmanite, Fp: Ferropericlasite). Model 1 considers the crystallization of the deep mantle as an assemblage of Ca-perovskite, bridgmanite and ferropericlasite. Model 2 considers the sequential crystallization of the upper mantle from the transition zone to the surface. Modal compositions are from Elkins-Tanton (2008). **B.** Variation of  $D^{\text{Lu}}/D^{\text{Hf}}$  and  $D^{\text{Sm}}/D^{\text{Nd}}$  with pressure and thus mineral assemblage. Open diamonds reflect the results of experimental studies at various pressures, with partition coefficients for individual phases combined in the shown mineral proportions to obtain the bulk D value. For simplicity, constant  $D^{\text{Lu}}/D^{\text{Hf}}$  and  $D^{\text{Sm}}/D^{\text{Nd}}$  values were used in the calculations for each interval; these are shown as vertical bars. Partitioning data are from Corgne et al. (2005, 2012), Draper et al. (2003) and Salters & Longhi (1999).

**Fig. 8.**  $^{147}\text{Sm}/^{144}\text{Nd}$  versus  $^{176}\text{Lu}/^{177}\text{Hf}$  produced by batch crystallization processes for Models 1 and 2. Squares are for cumulates and circles are for the residual melt. These results are compared with the Nulliak depleted mantle source (red star). **(A)** Results for model 1. Each color represents a proportion of Ca-Perovskite (CaPv) in the mineralogical assemblage. The impact of trapped liquid (TL) in the assemblage is presented in this Figure. The proportion of trapped liquid varies from 0 to 30% with an incremental step of 5%. **(B)** Results for model 2. For each layer, the  $^{147}\text{Sm}/^{144}\text{Nd}$  versus  $^{176}\text{Lu}/^{177}\text{Hf}$  of the starting liquid are those of the residual liquid produced by total crystallization of the underlying layer (with the exception of the bottom layer, which starts with a liquid having chondritic ratios Lu/Hf and Sm/Nd). This diagram shows only the results for pure cumulates generated by batch crystallization, because the high Sm/Nd and Lu/Hf of these cumulates require large scales for the x and y-axes.

**Fig. 9.** Effect of retention of trapped liquid on  $^{147}\text{Sm}/^{144}\text{Nd}$  versus  $^{176}\text{Lu}/^{177}\text{Hf}$  compositions of cumulates formed by batch sequential crystallization of the upper mantle (Model 2). The proportion of trapped liquid considered ranges between 5 and 30% (with 5% increments), and is assumed to remain constant during the crystallization process. Pressure ranges of the corresponding layer are indicated in each of the six panels.

707

## 708       **References**

- 709       Bennett V. C., Brandon A. D. and Nutman A. P. (2007) Coupled  $^{142}\text{Nd}$ - $^{143}\text{Nd}$  isotopic evidence for Hadean  
710       mantle dynamics. *Science* **318**, 1907–1910.
- 711       Blichert-toft J. (2001) On the Lu-Hf Isotope Geochemistry of Silicate Rocks. *Geostand. Newsl.* **25**, 41–56.
- 712       Blichert-Toft J., Arndt N. T., Wilson A. and Coetzee G. (2015) Hf and Nd isotope systematics of early Archean  
713       komatiites from surface sampling and ICDP drilling in the Barberton Greenstone Belt, South Africa. *Am.*  
714       *Mineral.* **100**, 2396–2411.
- 715       Blichert-Toft J., Chauvel C. and Albarède F. (1997) Separation of Hf and Lu for high-precision isotope analysis  
716       of rock samples by magnetic sector-multiple collector ICP-MS. *Contrib. to Mineral. Petrol.* **127**, 248–260.
- 717       Borg L. E., Connelly J. N., Boyet M. and Carlson R. W. (2011) Chronological evidence that the Moon is either  
718       young or did not have a global magma ocean. *Nature* **477**, 70–72. Available at:  
719       <http://dx.doi.org/10.1038/nature10328>.
- 720       Borg L. E. and Draper D. S. (2003) A petrogenetic model for the origin and compositional variation of the  
721       martian basaltic meteorites. *Meteorit. Planet. Sci.* **38**, 1713–1731. Available at:  
722       <http://doi.wiley.com/10.1111/j.1945-5100.2003.tb00011.x>.
- 723       Bourdon B. and Caro G. (2007) The early terrestrial crust. *Comptes Rendus - Geosci.* **339**, 928–936.
- 724       Bouvier A., Vervoort J. D. and Patchett P. J. (2008) The Lu-Hf and Sm-Nd isotopic composition of CHUR:  
725       Constraints from unequilibrated chondrites and implications for the bulk composition of terrestrial planets.  
726       *Earth Planet. Sci. Lett.* **273**, 48–57.
- 727       Boyet M. and Carlson R. W. (2007) A highly depleted moon or a non-magma ocean origin for the lunar crust?  
728       *Earth Planet. Sci. Lett.* **262**, 505–516.
- 729       Bridgwater D. and Schiøtte L. (1991) The Archean gneiss complex of northern Labrador: A review of current  
730       results, ideas and problems. *Bull. Geol. Soc. Denmark* **39**, 153–166. Available at:  
731       <http://scholar.google.com/scholar?hl=en&btnG=Search&q=intitle:The+Archean+gneiss+complex+of+nort>  
732       [hern+Labrador:+A+review+of+current+results,+ideas+and+problems#0](http://scholar.google.com/scholar?hl=en&btnG=Search&q=intitle:The+Archean+gneiss+complex+of+northern+Labrador:+A+review+of+current+results,+ideas+and+problems#0).
- 733       Brown S. M., Elkins-Tanton L. T. and Walker R. J. (2014) Effects of magma ocean crystallization and overturn  
734       on the development of  $^{142}\text{Nd}$  and  $^{182}\text{W}$  isotopic heterogeneities in the primordial mantle. *Earth Planet.*  
735       *Sci. Lett.* **408**, 319–330. Available at: <http://linkinghub.elsevier.com/retrieve/pii/S0012821X14006463>.
- 736       Canup R. M. (2004) Simulations of a late lunar-forming impact. *Icarus* **168**, 433–456.
- 737       Canup R. M. and Asphaug E. (2001) Origin of the Moon in a giant impact near the end of the Earth's formation.  
738       *Nature* **412**, 708–712.
- 739       Caracausi A., Avice G., Burnard P. G., Füre E. and Marty B. (2016) Chondritic xenon in the Earth's mantle.  
740       *Nature* **533**.
- 741       Caro G., Bourdon B. and Birck J. (2003)  $^{146}\text{Sm}$  –  $^{142}\text{Nd}$  evidence from Isua metamorphosed sediments for  
742       early differentiation of the Earth's mantle. *Nature* **423**.
- 743       Caro G., Bourdon B., Birck J. L. and Moorbath S. (2006) High-precision  $^{142}\text{Nd}/^{144}\text{Nd}$  measurements in  
744       terrestrial rocks: Constraints on the early differentiation of the Earth's mantle. *Geochim. Cosmochim. Acta*  
745       **70**, 164–191.
- 746       Caro G., Bourdon B., Wood B. J. and Corgne A. (2005) Trace-element fractionation in Hadean mantle generated  
747       by melt segregation from a magma ocean. *Nature* **436**, 246–249.
- 748       Caro G., Morino P., Mojzsis S. J., Cates N. L. and Bleeker W. (2017) Sluggish Hadean geodynamics: Evidence

749 from coupled 146,147Sm-142,143Nd systematics in Eoarchean supracrustal rocks of the Inukjuak domain  
750 (Québec). *Earth Planet. Sci. Lett.* **457**, 23–37. Available at: <http://dx.doi.org/10.1016/j.epsl.2016.09.051>.

751 Chambers J. E. (2004) Planetary accretion in the inner Solar System. *Earth Planet. Sci. Lett.* **223**, 241–252.  
752 Available at: <http://linkinghub.elsevier.com/retrieve/pii/S0012821X04002791> [Accessed October 20,  
753 2016].

754 Chambers J. E. and Wetherill G. W. (1998) Making the Terrestrial Planets: N-Body Integrations of Planetary  
755 Embryos in Three Dimensions. *Icarus* **136**, 304–327. Available at:  
756 <http://linkinghub.elsevier.com/retrieve/pii/S0019103598960079> [Accessed October 20, 2016].

757 Chauvel C., Lewin E., Carpentier M., Arndt N. T. and Marini J.-C. (2008) Role of recycled oceanic basalt and  
758 sediment in generating the Hf–Nd mantle array. *Nat. Geosci.* **1**, 64–67.

759 Coltice N., Moreira M., Hernlund J. and Labrosse S. (2011) Crystallization of a basal magma ocean recorded by  
760 Helium and Neon. *Earth Planet. Sci. Lett.* **308**, 193–199. Available at:  
761 <http://dx.doi.org/10.1016/j.epsl.2011.05.045>.

762 Connelly J. N. and Bizzarro M. (2016) Lead isotope evidence for a young formation age of the Earth–Moon  
763 system. *Earth Planet. Sci. Lett.* **452**, 36–43. Available at:  
764 <http://linkinghub.elsevier.com/retrieve/pii/S0012821X16303582> [Accessed October 19, 2016].

765 Corgne A. (2004) Silicate perovskite – melt partitioning of trace elements and geochemical signature of a deep  
766 perovskitic reservoir Electronic annex EA1 Table EA1 . Compositions ( in ppm ) of perovskite and  
767 coexist. **2738**.

768 Corgne A., Armstrong L. S., Keshav S., Fei Y., McDonough W. F., Minarik W. G. and Moreno K. (2012) Trace  
769 element partitioning between majoritic garnet and silicate melt at 10-17GPa: Implications for deep mantle  
770 processes. *Lithos* **148**, 128–141. Available at: <http://dx.doi.org/10.1016/j.lithos.2012.06.013>.

771 Corgne A., Liebske C., Wood B. J., Rubie D. C. and Frost D. J. (2004) Silicate perovskite-melt partitioning of  
772 trace elements and geochemical signature of a deep perovskitic reservoir. *Geochim. Cosmochim. Acta* **69**,  
773 485–496.

774 Corgne A. and Wood B. J. (2004) Trace element partitioning between majoritic garnet and silicate melt at 25  
775 GPa. *Phys. Earth Planet. Inter.* **143**, 407–419.

776 Debaille V., O'Neill C., Brandon A. D., Haenecour P., Yin Q. Z., Mattielli N. and Treiman A. H. (2013)  
777 Stagnant-lid tectonics in early Earth revealed by 142Nd variations in late Archean rocks. *Earth Planet. Sci.*  
778 *Lett.* **373**, 83–92. Available at: <http://dx.doi.org/10.1016/j.epsl.2013.04.016>.

779 Debaille V., Yin Q. Z., Brandon a. D. and Jacobsen B. (2008) Martian mantle mineralogy investigated by the  
780 176Lu-176Hf and 147Sm-143Nd systematics of shergottites. *Earth Planet. Sci. Lett.* **269**, 186–199.

781 Draper D. S., Xirouchakis D. and Agee C. B. (2003) Trace element partitioning between garnet and chondritic  
782 melt from 5 to 9 GPa: Implications for the onset of the majorite transition in the martian mantle. *Phys.*  
783 *Earth Planet. Inter.* **139**, 149–169.

784 Elkins-Tanton L. T. (2008) Linked magma ocean solidification and atmospheric growth for Earth and Mars.  
785 *Earth Planet. Sci. Lett.* **271**, 181–191.

786 Elkins-Tanton L. T., Burgess S. and Yin Q. Z. (2011) The lunar magma ocean: Reconciling the solidification  
787 process with lunar petrology and geochronology. *Earth Planet. Sci. Lett.* **304**, 326–336. Available at:  
788 <http://dx.doi.org/10.1016/j.epsl.2011.02.004>.

789 Elkins-Tanton L. T., Parmentier E. M. and Hess P. C. (2003) Magma ocean fractional crystallization and  
790 cumulate overturn in terrestrial planets: Implications for Mars. *Meteorit. Planet. Sci.* **38**, 1753–1771.

791 Elkins-Tanton L. T., Zaranek S. E., Parmentier E. M. and Hess P. C. (2005) Early magnetic field and magmatic  
792 activity on Mars from magma ocean cumulate overturn. *Earth Planet. Sci. Lett.* **236**, 1–12.

793 Fletcher I. R. and Rosman K. J. R. (1982) Precise determination of initial  $\epsilon_{\text{Nd}}$  from Sm-Nd isochron data.  
794 *Geochim. Cosmochim. Acta* **46**, 1983–1987. Available at:

- 795 <http://linkinghub.elsevier.com/retrieve/pii/0016703782901387> [Accessed October 19, 2016].
- 796 Guitreau M., Blichert-Toft J., Mojzsis S. J., Roth A. S. G. and Bourdon B. (2013) A legacy of Hadean silicate  
797 differentiation inferred from Hf isotopes in Eoarchean rocks of the Nuvvuagittuq supracrustal belt  
798 (Québec, Canada). *Earth Planet. Sci. Lett.* **362**, 171–181. Available at:  
799 <http://linkinghub.elsevier.com/retrieve/pii/S0012821X12006814>.
- 800 Hoffmann J. E., Münker C., Polat A., König S., Mezger K. and Rosing M. T. (2010) Highly depleted Hadean  
801 mantle reservoirs in the sources of early Archean arc-like rocks, Isua supracrustal belt, southern West  
802 Greenland. *Geochim. Cosmochim. Acta* **74**, 7236–7260. Available at:  
803 <http://linkinghub.elsevier.com/retrieve/pii/S0016703710005405>.
- 804 Hoffmann J. E., Münker C., Polat A., Rosing M. T. and Schulz T. (2011) The origin of decoupled Hf-Nd isotope  
805 compositions in Eoarchean rocks from southern West Greenland. *Geochim. Cosmochim. Acta* **75**, 6610–  
806 6628.
- 807 Hoffmann J. E. and Wilson A. H. (2016) The origin of highly radiogenic Hf isotope compositions in 3.33Ga  
808 Commondale komatiite lavas (South Africa). *Chem. Geol.* **455**, 6–21. Available at:  
809 <http://dx.doi.org/10.1016/j.chemgeo.2016.10.010>.
- 810 Irifune T. (1994) Absence of an aluminous phase in the upper part of the Earth's lower mantle. *Nature* **370**, 131–  
811 133. Available at:  
812 <http://www.nature.com/doi/10.1038/370131a0>  
813 <http://www.nature.com/nature/journal/v370/n6485/abs/370131a0.html>  
<http://dx.doi.org/10.1038/370131a0>.
- 814 Komiya T., Yamamoto S., Aoki S., Sawaki Y., Ishikawa A., Tashiro T., Koshida K., Shimojo M., Aoki K. and  
815 Collerson K. D. (2015) Geology of the Eoarchean, >3.95Ga, Nulivik supracrustal rocks in the Saglek  
816 Block, northern Labrador, Canada: The oldest geological evidence for plate tectonics. *Tectonophysics*.  
817 Available at: <http://linkinghub.elsevier.com/retrieve/pii/S0040195115002693>.
- 818 Labrosse S., Hernlund J. W. and Coltice N. (2007) A crystallizing dense magma ocean at the base of the Earth's  
819 mantle. *Nature* **450**, 866–869.
- 820 Lagos M., Ballhaus C., Münker C., Wohlgemuth-Ueberwasser C., Berndt J. and Kuzmin D. V. (2008) The  
821 Earth's missing lead may not be in the core. *Nature* **456**, 89–92.
- 822 Luais B., Le Carlier de Veslud C., Géraud Y. and Gauthier-Lafaye F. (2009) Comparative behavior of Sr, Nd  
823 and Hf isotopic systems during fluid-related deformation at middle crust levels. *Geochim. Cosmochim.*  
824 *Acta* **73**, 2961–2977.
- 825 Ludwig K. (2012) Isoplot version 3.75–4.15: a geochronological toolkit for Microsoft. *Excel Berkley*  
826 *Geochronological Cent. Spec. Publ.*
- 827 McLeod C. L., Brandon A. D. and Armytage R. M. G. (2014) Constraints on the formation age and evolution of  
828 the Moon from <sup>142</sup>Nd–<sup>143</sup>Nd systematics of Apollo 12 basalts. *Earth Planet. Sci. Lett.* **396**, 179–189.  
829 Available at: <http://dx.doi.org/10.1016/j.epsl.2014.04.007>.
- 830 Morbidelli A., Lunine J. I., O'Brien D. P., Raymond S. N. and Walsh K. J. (2012) Building Terrestrial Planets.  
831 *Annu. Rev. Earth Planet. Sci.* **40**, 251–275. Available at:  
832 <http://www.annualreviews.org/doi/10.1146/annurev-earth-042711-105319>.
- 833 Morino P., Caro G., Reisberg L. and Schumacher A. (2017) Chemical stratification in the post-magma ocean  
834 Earth inferred from coupled <sup>146</sup>Sm–<sup>142</sup>Nd systematics in ultramafic rocks of the Saglek block  
835 (3.25–3.9 Ga; northern Labrador, Canada). *Earth Planet. Sci. Lett.* **463**, 136–150. Available at:  
836 <http://linkinghub.elsevier.com/retrieve/pii/S0012821X17300560>.
- 837 Mukhopadhyay S. (2012) Early differentiation and volatile accretion recorded in deep-mantle neon and xenon.  
838 *Nature* **486**, 101–4. Available at: <http://www.ncbi.nlm.nih.gov/pubmed/22678288> [Accessed October 25,  
839 2016].
- 840 Mundl A., Touboul M., Jackson M. G., Day J. M. D., Kurz M. D., Lekic V., Helz R. T. and Walker R. J. (2017)  
841 Tungsten-182 heterogeneity in modern ocean island basalts. *Science (80-. )*. **356**, 66–69.

842 Munker C, Weyer S, Scherer E and Mezger K (2001) Separation of high field strength elements (Nb, Ta, Zr, Hf)  
843 and Lu from rock samples for MC-IPMS measurements. *Geochemistry Geophys. Geosystems* **2**.

844 Nesbitt R. W. and Su S. (1979) Komatiites: Geochemistry and Genesis. *Can. Mineral.* **17**, 165–186.

845 O’Neil J., Rizo H., Boyet M., Carlson R. W. and Rosing M. T. (2016) Geochemistry and Nd isotopic  
846 characteristics of Earth’s Hadean mantle and primitive crust. *Earth Planet. Sci. Lett.* **442**, 194–205.  
847 Available at: <http://dx.doi.org/10.1016/j.epsl.2016.02.055>.

848 O’Neill C. and Debaille V. (2014) The evolution of Hadean–Eoarchaeon geodynamics. *Earth Planet. Sci. Lett.*  
849 **406**, 49–58. Available at: <http://linkinghub.elsevier.com/retrieve/pii/S0012821X14005408>.

850 Ohtani E. (1985) The primordial terrestrial magma ocean and its implication for stratification of the mantle. *Phys.*  
851 *Earth Planet. Inter.* **38**, 70–80.

852 Oversby V. M. and Ringwood A. E. (1971) Time of Formation of the Earth’s Core. *Nature* **234**, 463–465.  
853 Available at: [http://adsabs.harvard.edu/cgi-bin/nph-](http://adsabs.harvard.edu/cgi-bin/nph-data_query?bibcode=1971Natur.234..463O&link_type=EJOURNAL%5Cnpapers3://publication/doi/10.1038/234463a0)  
854 [data\\_query?bibcode=1971Natur.234..463O&link\\_type=EJOURNAL%5Cnpapers3://publication/doi/10.10](http://adsabs.harvard.edu/cgi-bin/nph-data_query?bibcode=1971Natur.234..463O&link_type=EJOURNAL%5Cnpapers3://publication/doi/10.1038/234463a0)  
855 [38/234463a0](http://adsabs.harvard.edu/cgi-bin/nph-data_query?bibcode=1971Natur.234..463O&link_type=EJOURNAL%5Cnpapers3://publication/doi/10.1038/234463a0).

856 Peters B. J., Carlson R. W., Day J. M. D. and Horan M. F. (2018) Hadean silicate differentiation preserved by  
857 anomalous <sup>142</sup>Nd/<sup>144</sup>Nd ratios in the Réunion hotspot source. *Nature* **555**, 89–93. Available at:  
858 <http://dx.doi.org/10.1038/nature25754>.

859 Puchtel I. S., Blichert-Toft J., Touboul M., Horan M. F. and Walker R. J. (2016) The coupled <sup>182</sup>W–<sup>142</sup>Nd  
860 record of early terrestrial mantle differentiation. *Geochemistry Geophys. Geosystems* **17**, 2168–2193.

861 Puchtel I. S., Blichert-Toft J., Touboul M., Walker R. J., Byerly G. R., Nisbet E. G. and Anhaeusser C. R. (2013)  
862 Insights into early Earth from Barberton komatiites: Evidence from lithophile isotope and trace element  
863 systematics. *Geochim. Cosmochim. Acta* **108**, 63–90. Available at:  
864 <http://dx.doi.org/10.1016/j.gca.2013.01.016>.

865 Puchtel I. S., Touboul M., Blichert-Toft J., Walker R. J., Brandon A. D., Nicklas R. W., Kulikov V. S. and  
866 Samsonov A. V. (2016) Lithophile and siderophile element systematics of Earth’s mantle at the Archean–  
867 Proterozoic boundary: Evidence from 2.4 Ga komatiites. *Geochim. Cosmochim. Acta* **180**, 227–255.

868 Rizo H., Boyet M., Blichert-toft J., Neil J. O., Rosing M. T. and Paquette J. (2012) The elusive Hadean enriched  
869 reservoir revealed by <sup>142</sup>Nd deficits in Isua Archean rocks. *Nature* **490**, 96–100. Available at:  
870 <http://dx.doi.org/10.1038/nature11565>.

871 Rizo H., Boyet M., Blichert-Toft J. and Rosing M. (2011) Combined Nd and Hf isotope evidence for deep-seated  
872 source of Isua lavas. *Earth Planet. Sci. Lett.* **312**, 267–279. Available at:  
873 <http://dx.doi.org/10.1016/j.epsl.2011.10.014>.

874 Rizo H., Walker R. J., Carlson R. W., Horan M. F., Mukhopadhyay S., Manthos V., Francis D. and Jackson M.  
875 G. (2016) Preservation of Earth-forming events in the tungsten isotopic composition of modern flood  
876 basalts. *Science (80-. )*. **352**.

877 Ryan B. and Martineau Y. (2012) *Revised and Coloured edition of 1992 map showing the Geology of the Saglék*  
878 *fjord - Hebron fjord area, Labrador (NTS 14L/2,3,6,7). Scale 1:100000. Newfoundland Department of*  
879 *Mines and Energy, Geological survey BRanch, Map 92-18B and Geological Survey of Ca.,*

880 Salters V. J. M. and Longhi J. (1999) Trace element partitioning during the initial stages of melting beneath mid-  
881 ocean ridges. *Earth Planet. Sci. Lett.* **166**, 15–30.

882 Salters V. J. M. and Stracke A. (2004) Composition of the depleted mantle. *Geochemistry, Geophys. Geosystems*  
883 **5**.

884 Salters V. J. M. and White W. M. (1998) Hf isotope constraints on mantle evolution. *Chem. Geol.* **145**, 447–460.

885 Scherer E., Munker C. and Mezger K. (2001) Calibration of the Lutetium–Hafnium Clock. **293**, 683–688.

886 Schiøtte L. (1989) U–Th–Pb ages of single zircons in Archean supracrustals from Nain Province, Labrador



887       canada. *Can. J. Earth Sci.* **26**, 2636–2644.

888       Schiøtte L., Compston W. and Bridgwater D. (1989) U–Th–Pb ages of single zircons in Archaean supracrustals  
889       from Nain Province, Labrador, Canada. *Can. J. Earth Sci.* **26**, 2636–2644. Available at:  
890       [http://www.nrc.ca/cgi-bin/cisti/journals/rp/rp2\\_abst\\_e?cjes\\_e89-224\\_26\\_ns\\_nf\\_cjes26-89](http://www.nrc.ca/cgi-bin/cisti/journals/rp/rp2_abst_e?cjes_e89-224_26_ns_nf_cjes26-89) [Accessed  
891       October 19, 2016].

892       Schiøtte L., Nutman A. P. and Bridgwater D. (1992) U–Pb ages of single zircons within “Upernavik”  
893       metasedimentary rocks and regional implications for the tectonic evolution of the Archaean Nain Province,  
894       Labrador. *Can. J. Earth Sci.* **29**, 260–276. Available at:  
895       <http://www.nrcresearchpress.com/doi/abs/10.1139/e92-024> [Accessed October 19, 2016].

896       Shimojo M., Yamamoto S., Sakata S., Yokoyama T. D., Maki K., Sawaki Y., Ishikawa A., Aoki K., Aoki S.,  
897       Koshida K., Tashiro T., Hirata T., Collerson K. D. and Komiya T. (2016) Occurrence and geochronology  
898       of the Eoarchean, ~3.9Ga, Iqaluk Gneiss in the Saglek Block, northern Labrador, Canada: Evidence for  
899       the oldest supracrustal rocks in the world. *Precambrian Res.* **278**, 218–243. Available at:  
900       <http://linkinghub.elsevier.com/retrieve/pii/S0301926816300316> [Accessed October 19, 2016].

901       Snyder G. A., Taylor L. A. and Neal C. R. (1992) A chemical model for generating the sources of mare basalts:  
902       Combined equilibrium and fractional crystallization of the lunar magmasphere. *Geochim. Cosmochim.*  
903       *Acta* **56**, 3809–3823.

904       Söderlund U., Patchett P. J., Vervoort J. D. and Isachsen C. E. (2004) The <sup>176</sup>Lu decay constant determined by  
905       Lu–Hf and U–Pb isotope systematics of Precambrian mafic intrusions. *Earth Planet. Sci. Lett.* **219**, 311–  
906       324.

907       Solomatov V. and Louis S. (2007) Magma Oceans and Primordial Mantle Differentiation. In *Treatise on*  
908       *geophysics* Elsevier B.V. pp. 91–119.

909       Solomatov V. S. and Moresi L. (1996) Stagnant lid convection on Venus. *J. Geophys. Res.* **101**, 4737–4753.

910       Solomon S. C. and Longhi J. (1977) Magma oceanography : 1. Thermal evolution. In *Proc. Lunar. Planet. Sci.*  
911       *Conf. 8th*, pp. 583–599.

912       Touboul M., Puchtel I. S. and Walker R. J. (2012) 182W Evidence for Long-Term Preservation of Early Mantle  
913       Differentiation Products. **305**, 1065–1069.

914       Vervoort J. D. (2015) Lu–Hf Dating: the Lu–Hf Isotope System. *Encyclopedia of Scientific Dating*  
915       *Methods (2015): 379-390*.

916       Vervoort J. D., Patchett P. J., Söderlund U. and Baker M. (2004) Isotopic composition of Yb and the  
917       determination of Lu concentrations and Lu/Hf ratios by isotope dilution using MC-ICPMS. *Geochemistry,*  
918       *Geophys. Geosystems* **5**.

919       Weis D., Kieffer B., Hanano D., Silva I. N., Barling J., Pretorius W., Maerschalk C. and Mattielli N. (2007) Hf  
920       isotope compositions of U.S. Geological survey reference materials. *Geochemistry, Geophys. Geosystems*  
921       **8**.

922       Wimpenny J. B., Amelin Y. and Yin Q. (2013) Precise determination of the Lu isotopic composition in rocks  
923       and minerals using multi-collector ICP-MS. *Anal. Chem.*, 1–8.

924       Wood B. J., Halliday A. N. and Rehkämper M. (2010) Volatile accretion history of the Earth. *Nature* **461**, 1227–  
925       1233.

926       Wood B. J., Walter M. J. and Wade J. (2006) Accretion of the Earth and segregation of its core. *Nature* **441**,  
927       825–833.

928       Yang Y. heng, Zhang H. fu, Chu Z. yin, Xie L. wen and Wu F. yuan (2010) Combined chemical separation of  
929       Lu, Hf, Rb, Sr, Sm and Nd from a single rock digest and precise and accurate isotope determinations of  
930       Lu–Hf, Rb–Sr and Sm–Nd isotope systems using Multi-Collector ICP-MS and TIMS. *Int. J. Mass*  
931       *Spectrom.* **290**, 120–126. Available at: <http://dx.doi.org/10.1016/j.ijms.2009.12.011>.

932

FIGURE .1

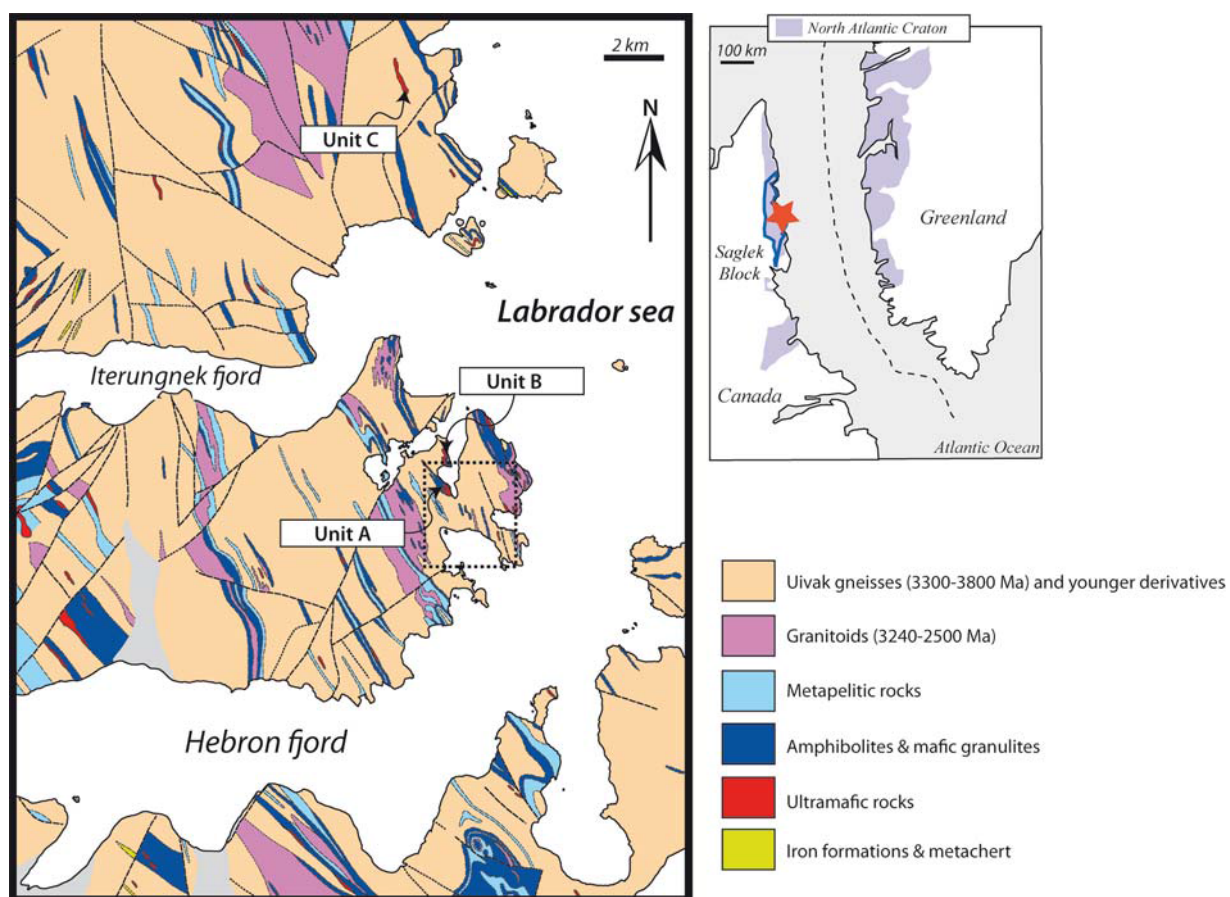


FIGURE 2

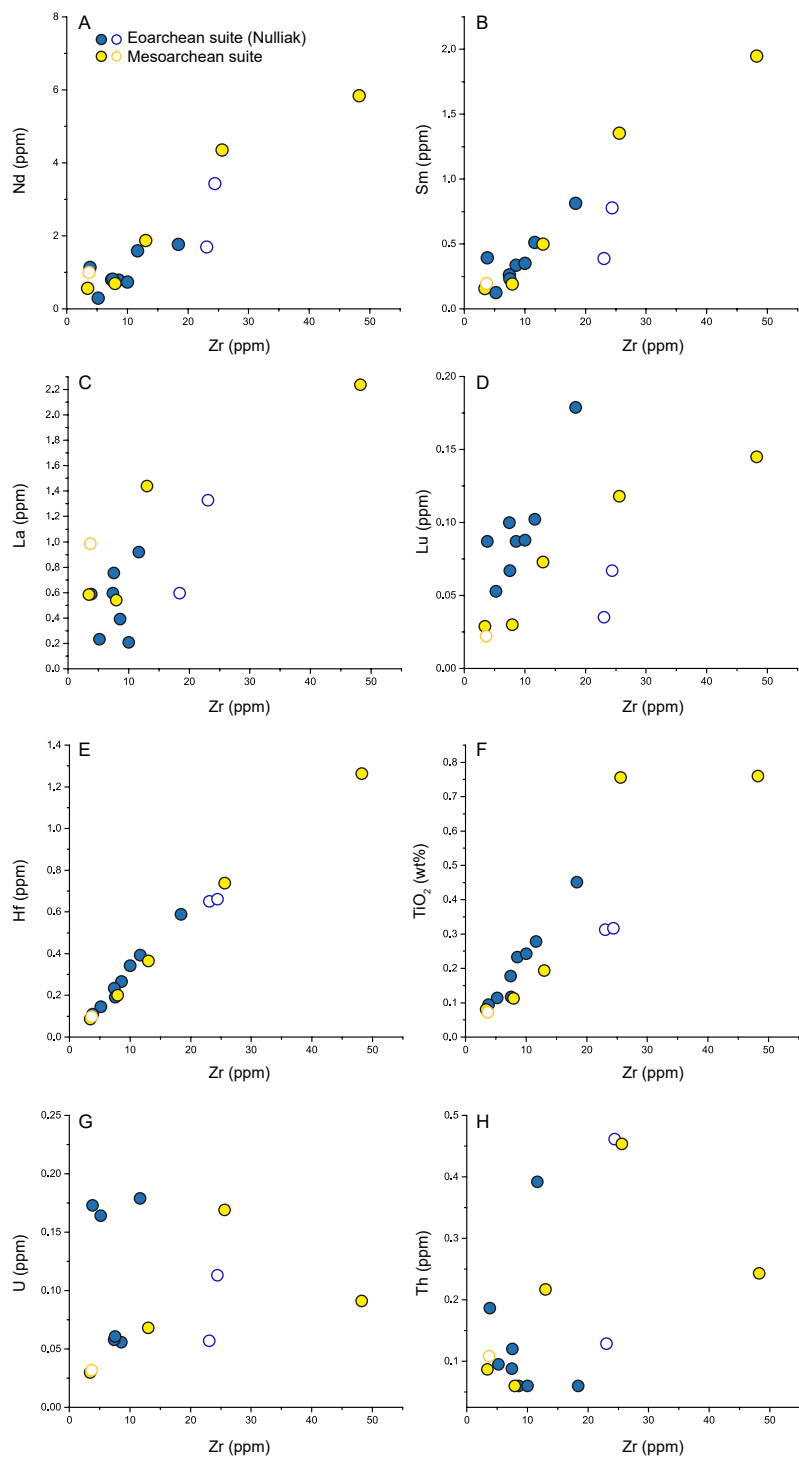


FIGURE 3

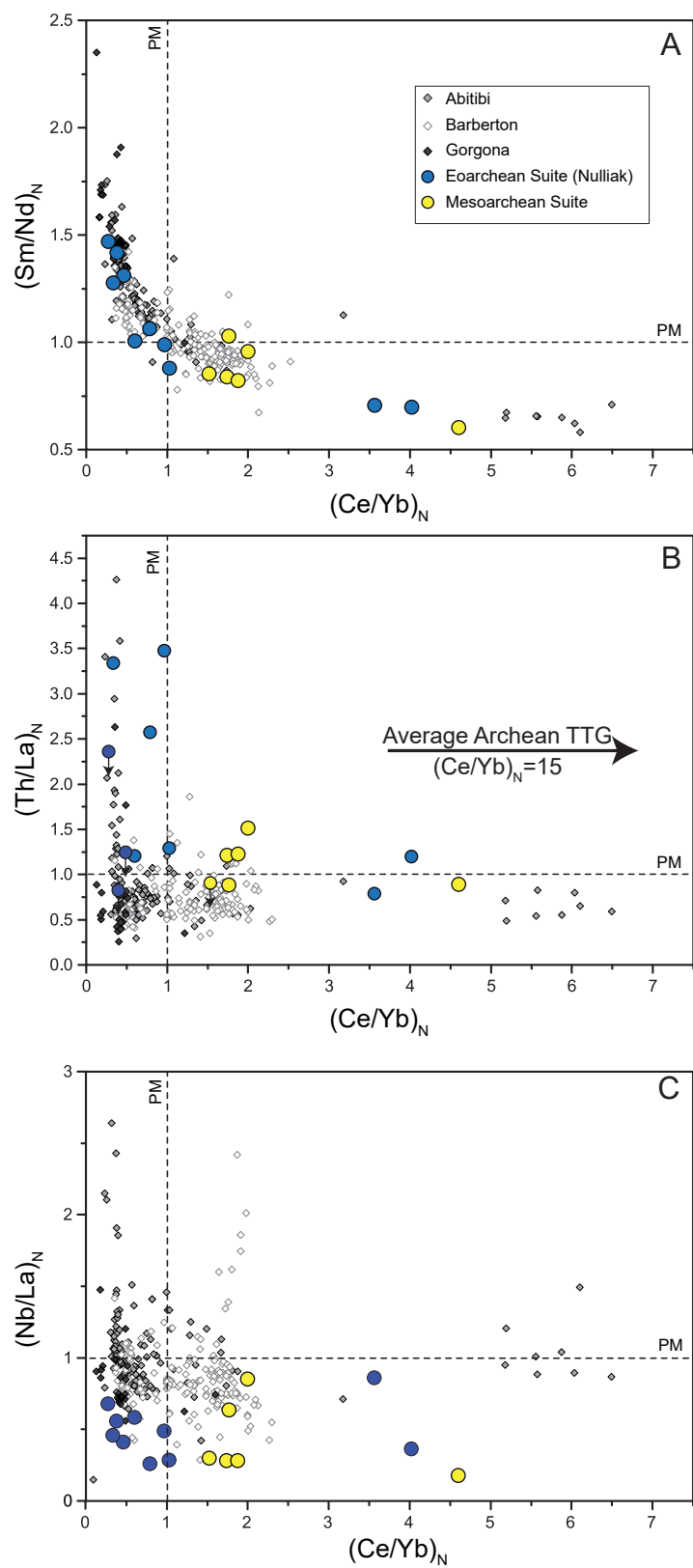


FIGURE 4

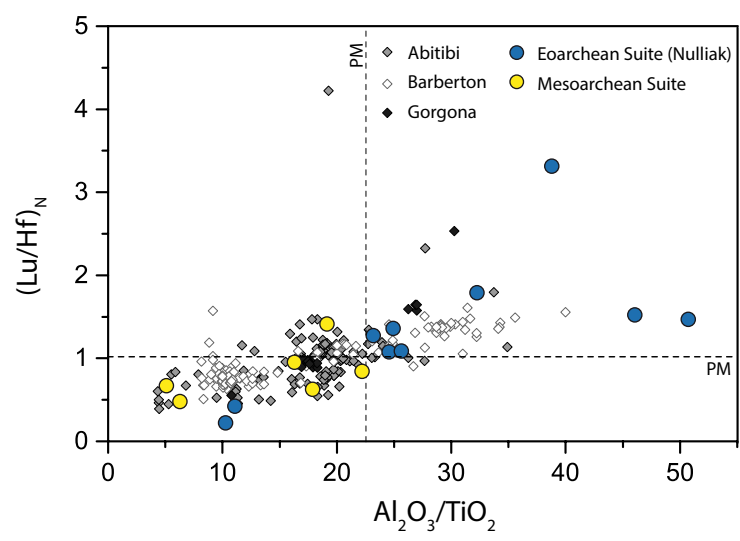


FIGURE 5.

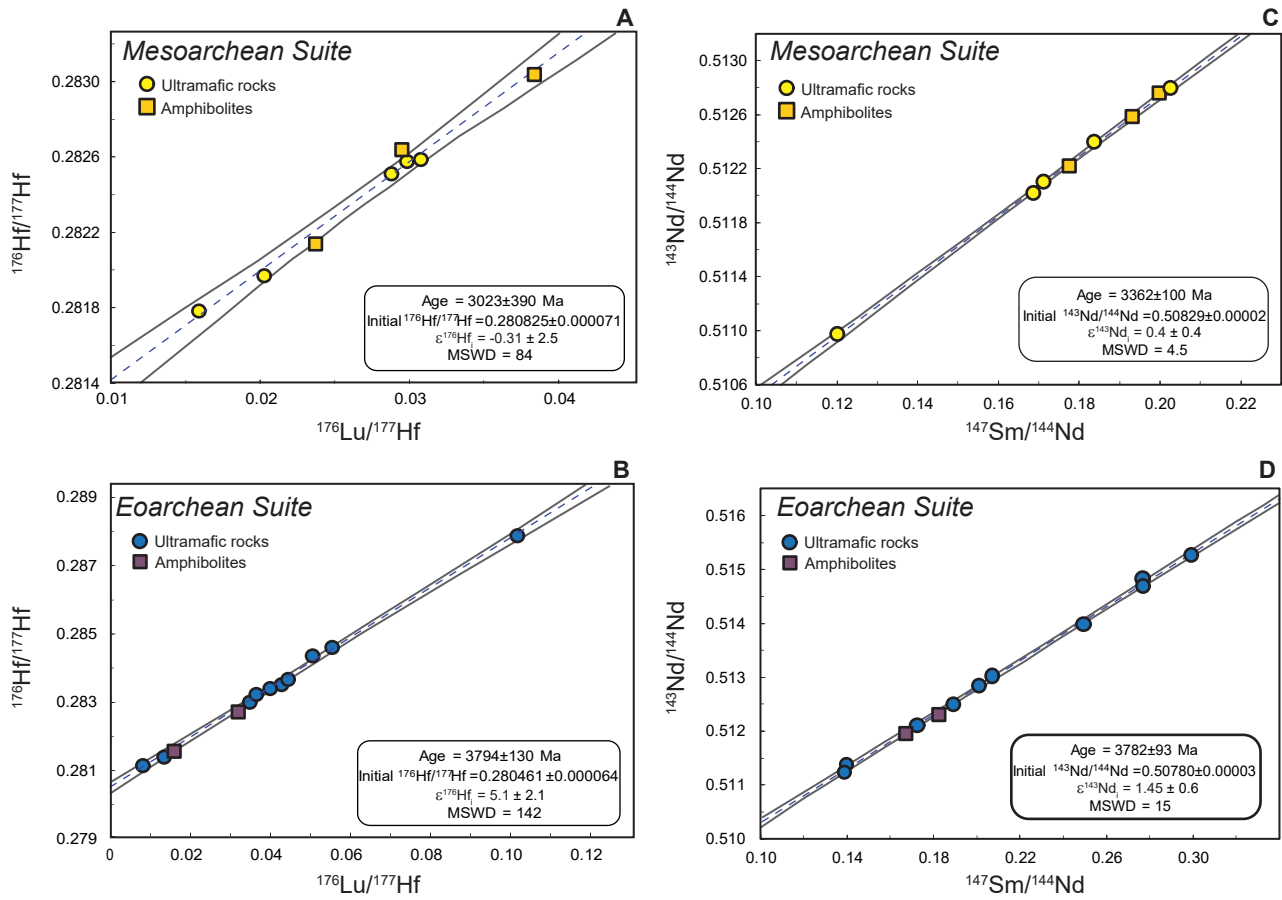


FIGURE 6.

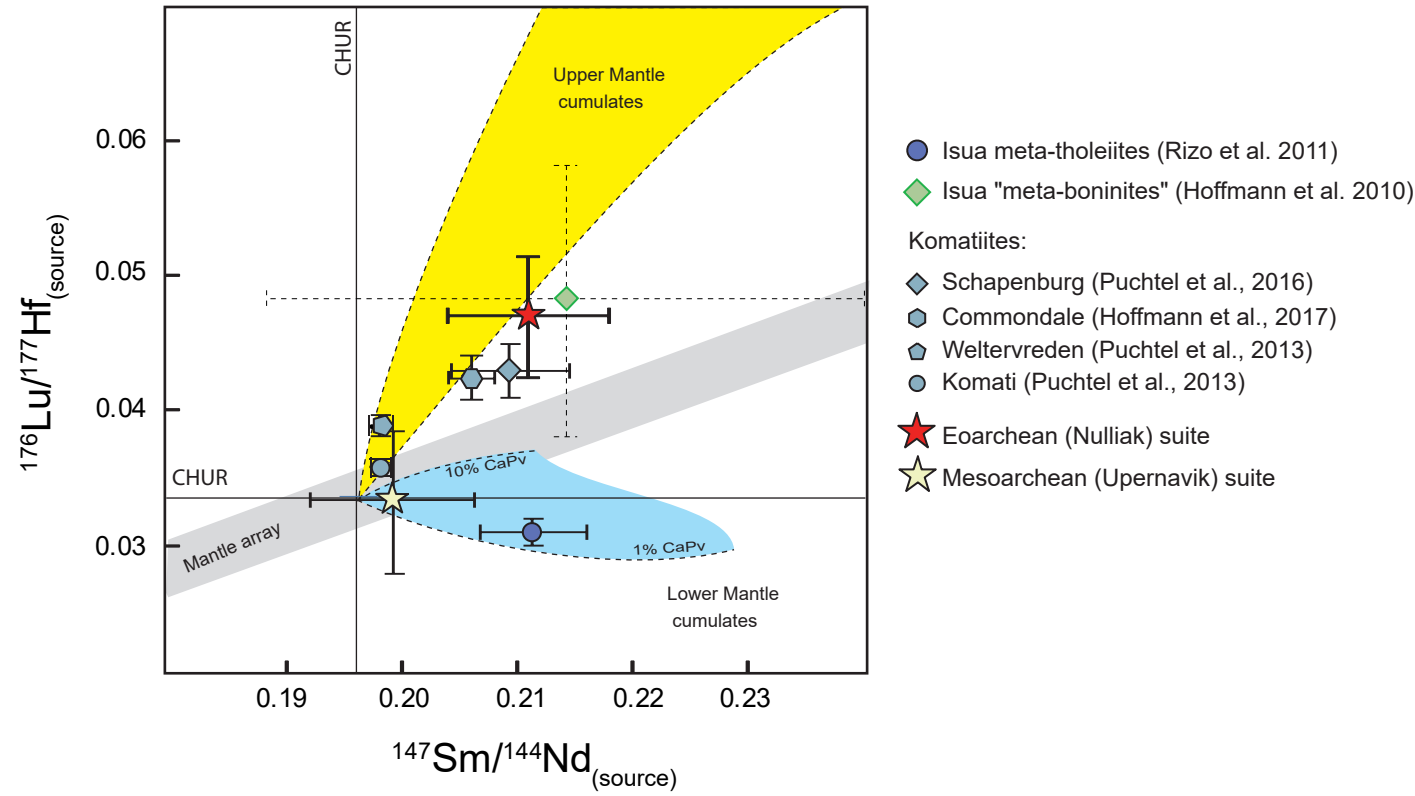


FIGURE 7.

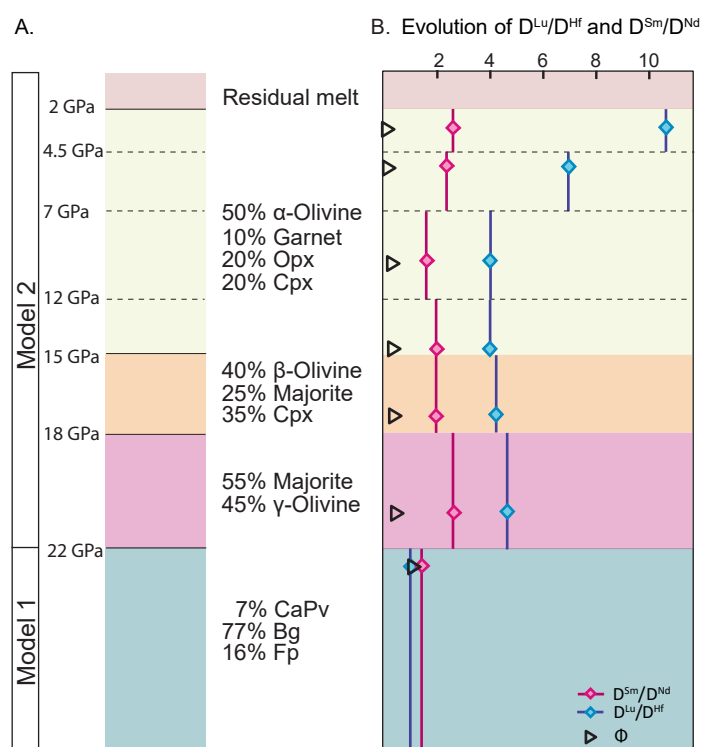




FIGURE 8.

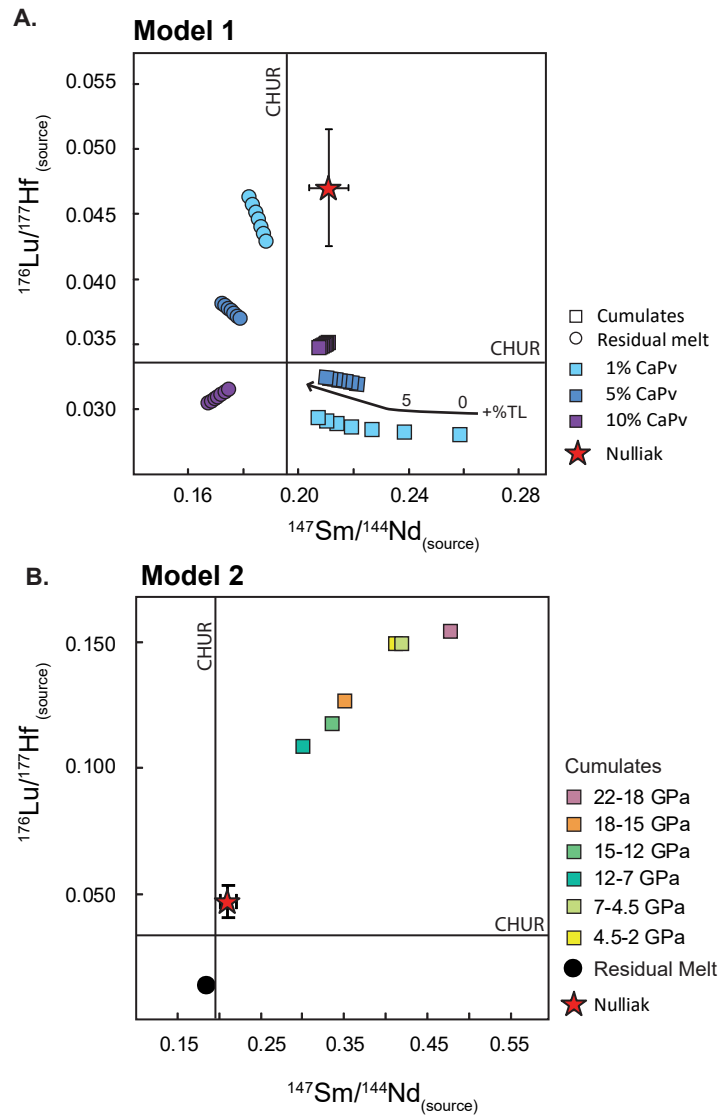


FIGURE 9

